

Durham E-Theses

Stroboscopic X-Ray topography of surface acoustic wave devices

Cringean, Janey Kirkpatrick

How to cite:

Cringean, Janey Kirkpatrick (1985) *Stroboscopic X-Ray topography of surface acoustic wave devices*, Durham theses, Durham University. Available at Durham E-Theses Online:
<http://etheses.dur.ac.uk/7238/>

Use policy

The full-text may be used and/or reproduced, and given to third parties in any format or medium, without prior permission or charge, for personal research or study, educational, or not-for-profit purposes provided that:

- a full bibliographic reference is made to the original source
- a [link](#) is made to the metadata record in Durham E-Theses
- the full-text is not changed in any way

The full-text must not be sold in any format or medium without the formal permission of the copyright holders.

Please consult the [full Durham E-Theses policy](#) for further details.

STROBOSCOPIC X-RAY TOPOGRAPHY
OF SURFACE ACOUSTIC WAVE DEVICES

by

JANEY KIRKPATRICK CRINGEAN B.Sc.

The copyright of this thesis rests with the author.
No quotation from it should be published without
his prior written consent and information derived
from it should be acknowledged.

A thesis submitted to the University of Durham in
candidature for the Degree of Master of Science.

August 1985



14 MAY 1987

Theris
1985/CRI

ABSTRACT

Stroboscopic X-ray topography using the time structure of synchrotron radiation has been used to investigate 38 MHz lithium niobate, LiNbO_3 , surface acoustic wave devices. The methods of topography are discussed with particular reference to synchrotron radiation and stroboscopic techniques. Surface acoustic wave devices are described and relevant aspects of their performance are discussed. A detailed review is given of previous investigations of surface acoustic wave devices, including investigation of the contrast mechanism of the imaging of surface acoustic waves. Experimental evidence relating to the performance of surface acoustic wave devices and to the interaction of surface acoustic waves with defects such as grain boundaries is discussed; it is suggested that the use of ultrasonic wave propagation theory could allow grain boundaries to be considered as infinitely thin cracks. The effects of input voltage and incident X-ray wavelength are investigated. Computer programs are presented which simulate image positions for stroboscopic investigations of lithium niobate and Laue patterns for cubic and hexagonal crystals. An assessment is made of the perfection of crystals of lithium tetraborate, $\text{Li}_2\text{B}_4\text{O}_7$, a possible future surface acoustic wave substrate material. Possibilities for future investigations are discussed.

ACKNOWLEDGEMENTS

Financial support from the Science and Engineering Research Council is acknowledged. I wish to express my gratitude to the Directors and staff of Daresbury Laboratory for the use of the facilities of the SRS, in particular to Dr G.F. Clark and Mr. C. Jackson for their help.

I thank Plessey Research (Caswell) Ltd. for financial assistance and Dr. R.W. Whatmore for provision of devices and crystals.

I am grateful to Dr. C.H. Emeleus for the use of the facilities of the Geology Department of the University of Durham.

I would like to thank Dr. B.K. Tanner for his supervision of this work. I am grateful for the assistance of all present members of the Solid State Group, including especially Mr. D.B. Lambrick and Mr. M.J. Hawton; Mr. I. MacLabhainn and Mr. R.M. Myers; the technical staff of the Physics Department, especially Mr. D. Oliver; and the staff of the library of the University of Durham.

Particular gratitude is extended to Dr. D.Y. Parpia, Mr. S.J. Barnett and Mr. M.J. Hill for many useful and interesting discussions and considerable practical assistance.

Finally, I thank my parents and brother for their assistance, encouragement and support.

CONTENTS

<u>CHAPTER AND TITLE</u>	<u>PAGE</u>
Chapter 1: X-ray Topography and Synchrotron Radiation	1
Chapter 2: Surface Acoustic Wave Devices	24
Chapter 3: Stroboscopic X-ray Topography Investigations of Surface Acoustic Wave Devices: A Review	35
Chapter 4: Experimental Investigations of Surface Acoustic Wave Devices	46
Chapter 5: Lithium Tetraborate	66
Chapter 6: Conclusions	80
References	83
Appendix A: Cuts of Lithium Niobate	87
Appendix B: Computer Program to Simulate Image Positions for Stroboscopic Investigations	89
Appendix C: Computer Programs to Simulate Back-reflection Laue Patterns for Cubic and Hexagonal Crystals	93
Appendix D: Computer Program to Calculate Extinction Distances for Lithium Tetraborate	98

CHAPTER 1: X-RAY TOPOGRAPHY AND SYNCHROTRON RADIATION

1.1 X-Ray Topography

The discovery of X-ray diffraction in 1912 served as the starting point for the development of scientific research along a number of important lines. However, it was not until the late 1950's that X-ray diffraction topography [1,2] of single crystals began to be developed. Since then, sufficiently perfect single crystals have become more widely available and experimental techniques have been elaborated. The methods of topography have acquired practical importance in crystal characterization and are now widely used for the assessment of crystal quality in a wide range of single crystal materials.

A great many types of inhomogeneity such as domain structures and impurity striations can be seen in topographs as well as crystallographic structure defects such as dislocations or grain boundaries. By choice of the appropriate techniques, as-grown crystals of any material that can be grown with sufficient perfection can be examined non-destructively. There are two aspects to the non-destructive nature of X-ray topography. Firstly, the X-rays will penetrate up to several millimetres in thickness of crystals containing only light elements; thus such crystals may be examined whole. Secondly, the X-ray



dosage received by a crystal in the course of its topographic examination is generally several orders of magnitude less than that required to produce detectable radiation damage.

X-ray topography complements the technique of electron microscopy [3]. X-ray topographs can be taken in transmission, with relatively low resolution, through large areas of crystal up to a few millimetres thick: electron microscopy can image only small areas of very thin material with high resolution. There are a number of different techniques of X-ray topography which can be classified according to whether the specimen is examined in transmission or reflection and whether the specimen is thick or thin. These have been reviewed by Lang [2] and Amelinckx [4].

The most popular and widely used technique of transmission X-ray topography is Lang's method [5], illustrated in Figure 1.1. Section topographs are taken with the crystal and film stationary and the beam narrow. Information on energy flow in the crystal may be obtained and the spatial distribution of defects is recorded. Projection topographs may be formed [6] by traversing the crystal and film together across the beam. Thus a line-by-line map of the intensity of the diffracted beam is recorded. This produces an image of the whole crystal although some information is lost in the process. The specimen thickness, t , and the X-ray wavelength are chosen

so that the relation $\mu t < 1$ is satisfied, where μ is the linear absorption coefficient for the monochromatic X-rays used. Transmission topography is termed the Laue case: reflection topography is termed the Bragg case. The latter [7] is possible using a beam reflected from the crystal rather than transmitted through it.

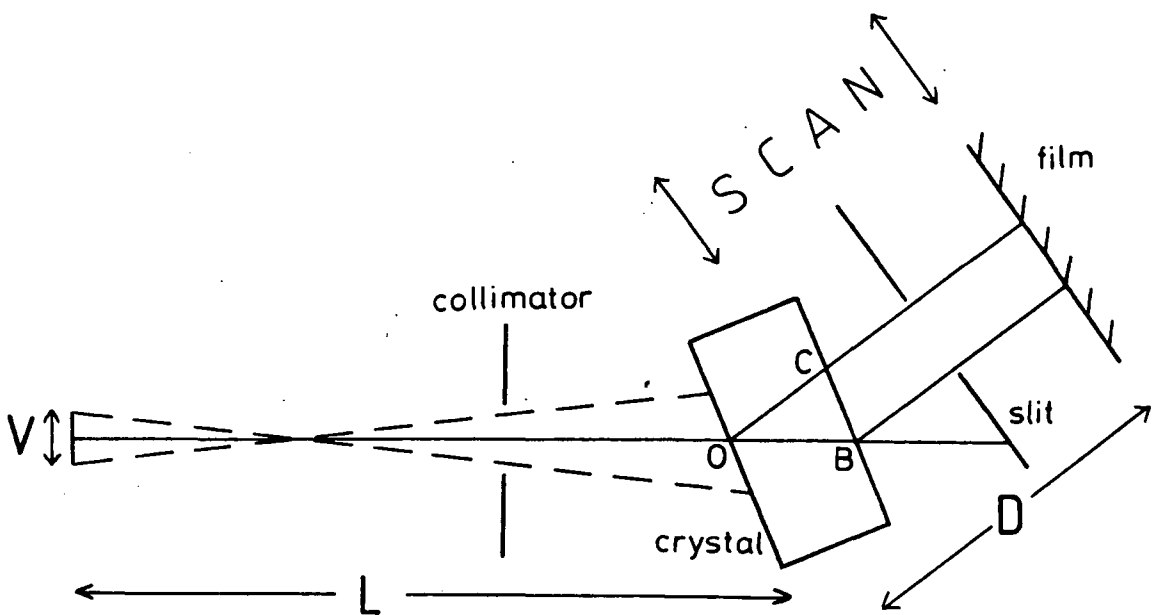


Figure 1.1: Lang's method for transmission topography. Section topographs correspond to the stationary situation; projection topographs are taken by scanning the crystal and film across the beam.

In Lang topography the criteria for resolution differ in the vertical and horizontal directions. The diffracting planes are vertical so there is essentially no diffraction in the vertical plane. The resolution, δ , is given by:

$$\delta = \frac{D V}{L}$$

where D is the specimen-plate distance, L is the source-specimen distance, and V is the projected height of the source (see Figure 1.1). Hence a small specimen-plate distance is desirable for good resolution. The divergence of the diffracted beam in the horizontal plane is very small and is not the limiting factor on resolution [1]. The resolution is usually of the order of a few microns.

X-ray topographs are normally recorded on Ilford L4 Nuclear Emulsion plates; it is widely accepted that these have excellent characteristics for high resolution topography. Other emulsions may be used but, although faster, have lower resolution. For optical applications a very thin emulsion would be chosen to obtain high resolution, but due to the relatively poor absorption of X-rays there is a limit to the minimum thickness tolerable. Generally 25 μm or 50 μm thickness is used for topography. Development is usually carried out near 0°C in order to reduce the development rate and so obtain uniform development. Topographs are recorded at a magnification of unity and subsequently enlarged optically.

The dynamical theory of diffraction [8] is required for the interpretation of details of contrast in X-ray topographs; this is complex and not fully developed. The kinematical theory, which assumes that the amplitudes of the scattered waves are small compared with the incident amplitude, is adequate for thin or imperfect crystals. However, for large single crystals that are also highly

perfect, multiple scattering of diffracted waves becomes important. Interchange of energy occurs between the incident and diffracted beams as they pass through the crystal, and it is necessary to account for the processes occurring.

The dynamical theory in the X-ray case has been excellently reviewed by Batterman and Cole [9] and by Authier [10]. Stated simply, it requires a solution of Maxwell's equations in a periodic medium matched to solutions which are plane waves outside the crystal.

Solutions inside the crystal must be Bloch waves [11] and these are normal modes since they propagate unchanged. They are of the form [1]:

$$D = \sum_{\underline{g}} D_{\underline{g}} \exp(-2\pi i \underline{K}_{\underline{g}} \cdot \underline{r}) \exp i \omega t$$

where ω is the angular frequency, the $D_{\underline{g}}$ are the component amplitudes of the wavefields, and the $\underline{K}_{\underline{g}}$ are related by the Laue condition:

$$\underline{K}_{\underline{g}} = \underline{K}_0 + \underline{g}$$

where \underline{g} is a reciprocal lattice vector. \underline{K}_0 and $\underline{K}_{\underline{g}}$ define the wavevectors of the components of the Bloch waves inside the crystal. For X-rays, because $|\underline{K}| \approx |\underline{g}|$, usually only one reflection is active at once. Substitution into Maxwell's equations and solution gives a relation between \underline{K}_0 and $\underline{K}_{\underline{g}}$. This defines the dispersion surface in reciprocal space, representing the values of the allowed wavevectors inside the crystal (see Figure 1.2). A point P on one of the dispersion surface branches is called a tie-point. Bloch

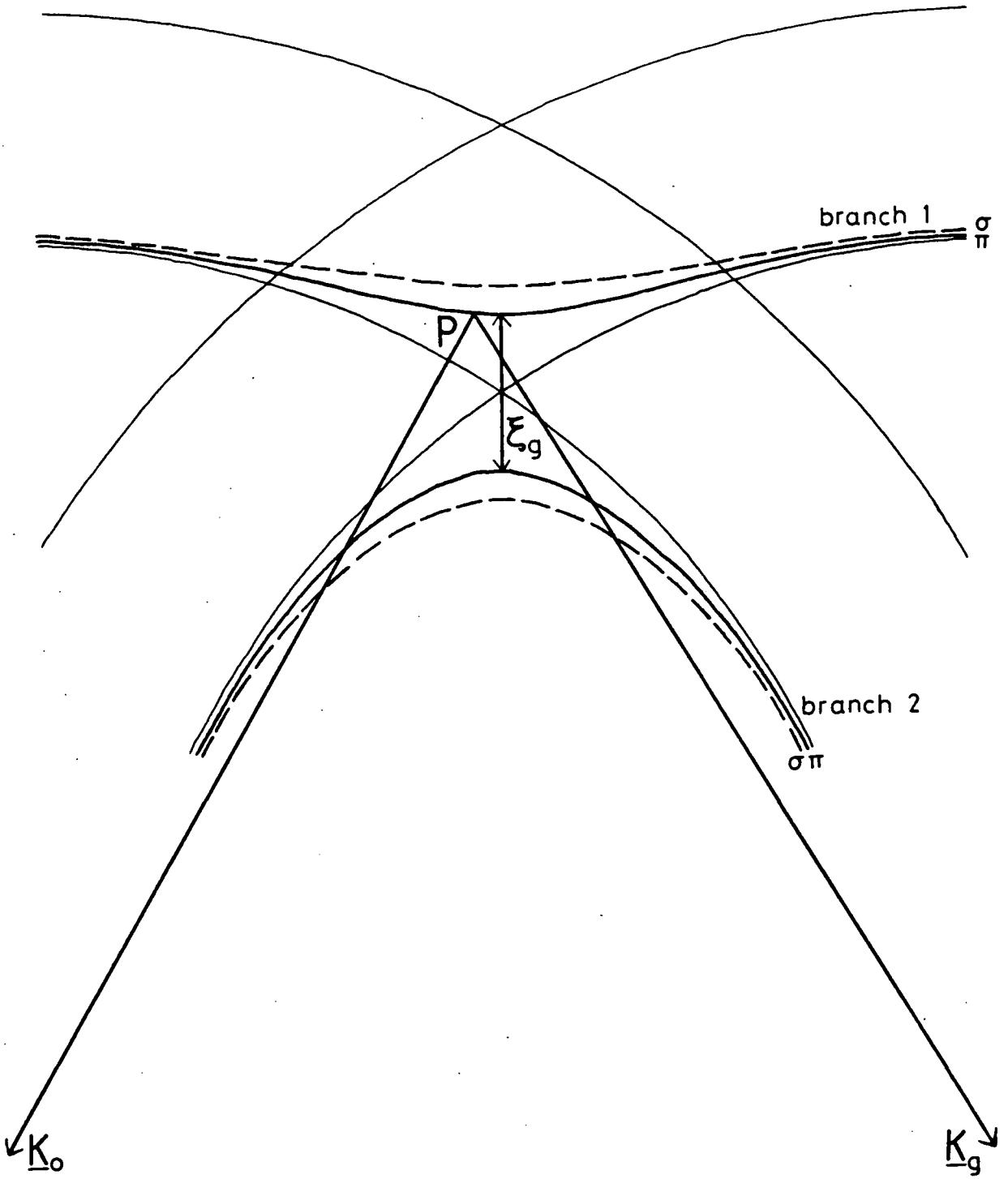


Figure 1.2: The dispersion surface of dynamical diffraction theory.

waves travel in real space in a direction perpendicular to the dispersion surface at the corresponding tie-point.

In single crystal topography the X-ray beam divergence is greater than the width of the dispersion surface diameter. All points along the dispersion surface are then simultaneously excited and X-rays propagate along all possible paths. In the plane of incidence these paths fill out a triangle OBC bordered by the incident and the reflected directions, OB and OC respectively (see Figure 1.1). This triangle is called the Borrmann fan.

Of critical importance in understanding diffraction contrast is the X-ray extinction distance, ξ_g , which is measured on a reciprocal scale as the minimum separation along the major axis of the branches of the dispersion surface (see Figure 1.2). It measures the thickness of the surface layer of crystal which contributes to the reflected beam in reflection topography. It is given by:

$$\xi_g = \frac{\pi V_c \cos \theta_B}{\lambda |F_g| C}$$

where V_c is the unit cell volume, θ_B is the Bragg angle and F_g the structure factor of the reflection using wavelength λ , and C is the polarization factor ($C=1$ for the σ polarization state, $C=\cos 2\theta_B$ for the π polarization state).

The extinction distance is used in the expression for the integrated intensity, which is given as:

$$I_g = \left(\frac{\pi}{2g\xi_g} \right) \int_0^{2\pi t/\xi_g} J_0(\theta) d\theta$$

where J_0 is the zero order Bessel function. The term outside the integral tells us that high-order reflections with long extinction distances give very low intensity; the integral determines how the intensity varies as a function of thickness. The intensity is an oscillatory function; the oscillations are the Pendellosung fringes which are normally observed in a wedge crystal, delineating contours of equal thickness [1]. However, as the thickness increases, the amplitude of the oscillations decreases and thus the visibility decreases.

The extinction distance can also be used to estimate dislocation image width. Dislocations [12,13] are line defects which can be specified by two vectors: the arbitrarily chosen positive direction along the dislocation line \underline{l} and the Burgers vector \underline{b} . A number of particular types of dislocations can be distinguished in terms of the angle between \underline{l} and \underline{b} - when the two vectors are parallel the dislocations are screw-type, and when \underline{l} and \underline{b} are at right angles the dislocations are edge-type. In some crystal structures other types of dislocations are significant. For screw dislocations, the total width of a dislocation image is given by:

$$s = \frac{\xi g}{2\pi} |\underline{g} \cdot \underline{b}|$$

The image of a pure edge dislocation, viewed in the reflection from the plane containing the line and normal to \underline{b} , is about 1.75 times the value given in the above

equation [14]. For weak reflections, for which ξ_g is large, large image widths are observed.

The X-ray intensity varies as the crystal is rotated through the Bragg condition. This dependence of intensity on angle is known as the rocking curve; if absorption is neglected this is a convolution of the perfect crystal reflecting curve, shown in Figure 1.3, and the divergence of the X-ray beam. In the geometrical situations of symmetrical transmission and symmetrical reflection from the crystal surface and under conditions when absorption is negligible, the expression for the angular range of reflection is:

$$W_0 = 2d\xi_g^{-1}$$

Here d is the interplanar spacing of the Bragg reflection concerned. W_0 is shown in Figure 1.3 for both cases.

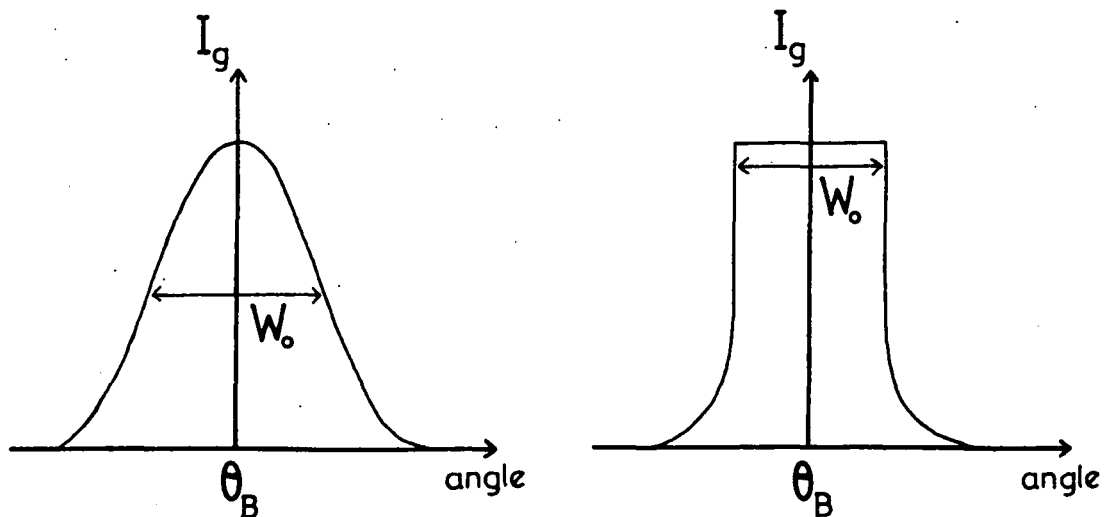


Figure 1.3: Perfect crystal reflecting curves for non-absorbing crystals.

- (a) For a moderately thick crystal in the Laue case. (b) For a thick crystal in the Bragg case.

The aim of all X-ray topographic methods is to provide information about the distribution of the defects in a crystal. X-ray images may be thought of as arising in two ways: orientation contrast and extinction contrast.

Orientation contrast can be manifested in two ways. Firstly, for a monochromatic beam, different reflected intensities occur for each subgrain within the crystal. If there is a misoriented area in the crystal, it will see the beam at a different glancing angle in the rocking curve and so different diffracted intensities will result. Secondly, if the beam is polychromatic there will be an overlap or separation of adjacent images because the different areas will diffract the beam in different directions.

Extinction contrast arises from a reduction of primary extinction in imperfect regions of the crystal. Primary extinction is the total reflection of X-rays by a perfect crystal in a certain region near the reflection maximum leading to rapid exponential damping of the waves in the crystal. It is this phenomenon which is responsible for the fact that the integrated intensity of reflection by a perfect crystal is proportional to the structure factor whereas the integrated intensity reflected by an imperfect crystal is proportional to the square of the structure factor. Hence, under conditions of extinction contrast, defects in otherwise perfect crystals cause localized increases in the reflected intensity and so appear in topographs as regions of greater intensity than the perfect

crystal background.

Three types of section topograph images have been characterized by Authier [15,16], as illustrated in Figure 1.4. At S the dislocation DD cuts the beam of X-rays which are not diffracted by the crystal. The deformed region around the dislocation line reflects intensity from this direct beam, giving rise to the "direct" image. As these X-rays are not diffracted by the perfect crystal they suffer no primary extinction and the direct image appears as an intense dark spot on section topographs.

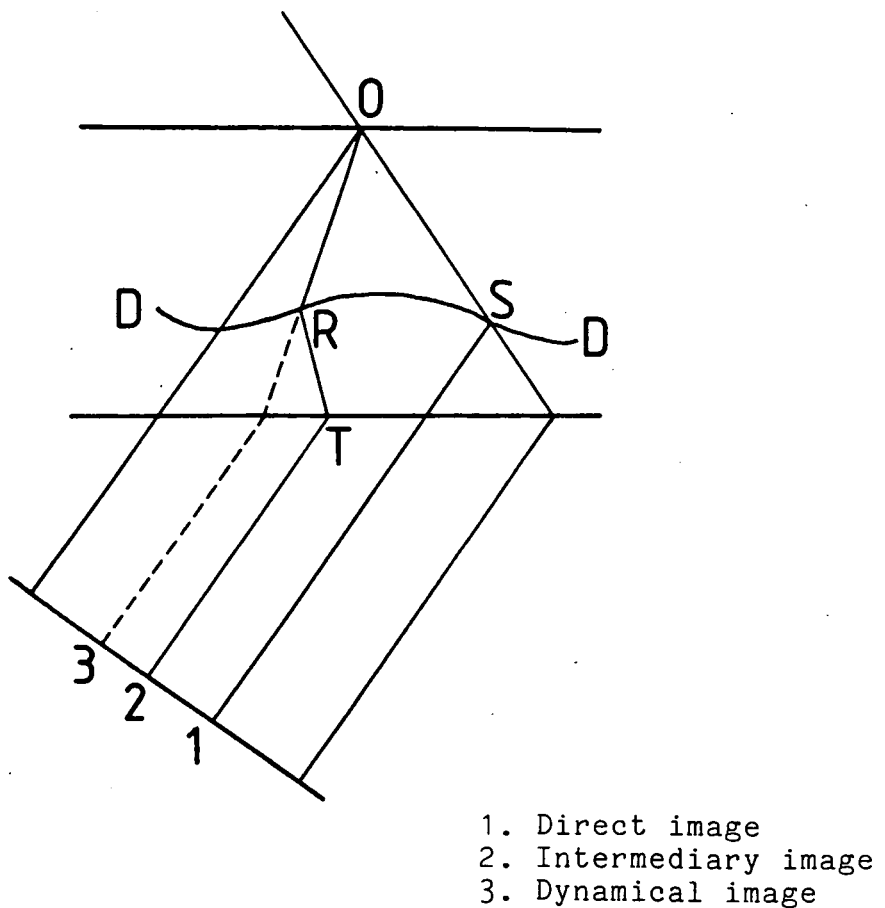


Figure 1.4: Principle of transmission topographs.

Within the Borrmann fan two types of image arise. On crossing the dislocation at R, wavefields propagating along OR decouple into their transmitted and diffracted components. When they re-enter perfect material they excite new wavefields. Intensity is removed from the direction OR and the dislocation casts a shadow known as the "dynamical" image; this is always less intense than the background. The newly created wavefields propagate along paths such as RT and these give rise to a third type of image, the "intermediary" image. Because the newly created wavefields interfere with the original wavefields, the intermediary image shows an oscillatory contrast. The Borrmann fan is filled with wavefields propagating in different directions; hence the dynamical and intermediary images have much poorer spatial resolution than the direct image.

Only when the Bragg planes are distorted are images observed. In a general isotropic elastic continuum the atomic displacement around a dislocation line, characterized by Burgers vector \underline{b} and line direction \underline{l} , in a plane normal to the line is [17]:

$$\underline{R}(r, \phi) = \frac{1}{2\pi} \underline{b}\phi + \underline{b}_e \frac{\sin 2\phi}{4(1-\nu)} + \underline{b} \times \underline{l} \left| \frac{1-2\nu}{2(1-\nu)} \ln r + \frac{\cos 2\phi}{4(1-\nu)} \right|$$

where \underline{b}_e is the edge component of the Burgers vector and ν is Poisson's ratio. When $\underline{g} \cdot \underline{R} = 0$, where \underline{g} is the reciprocal lattice vector normal to the hkl planes for the operative reflection, no contrast is observed from the defect in topographs because the Bragg planes are not distorted. For a pure screw dislocation, $\underline{R}(r, \phi) = \underline{b}\phi/2\pi$

and hence when

$$\frac{\underline{g} \cdot \underline{b}}{2 \phi} = 0$$

the dislocation is invisible. Similarly, for an edge dislocation we need $\underline{g} \cdot \underline{b} = 0$ and $\underline{g} \cdot \underline{b} \times \underline{l} = 0$ for invisibility, but the images are visually quite weak if only $\underline{g} \cdot \underline{b} = 0$. Defects can be identified by observing the contrast in a number of reflections and finding several non-coplanar \underline{g} vectors for which $\underline{g} \cdot \underline{b} = 0$. Thus X-ray topography thus allows identification of dislocations and characterization of crystals. This is discussed further in Chapter 5.

One of the drawbacks of X-ray topography is that exposure times are long in the laboratory. The advent of synchrotron radiation has reduced exposure times and has increased the potential of topography to include investigations previously impossible in the laboratory; this makes it a more powerful technique for crystal characterization.

1.2 Synchrotron Radiation

When electrons are deflected, for example by a magnetic field, they emit synchrotron radiation. This can be used in a wide range of experiments in materials science, surface, solid state, atomic, and molecular physics, crystallography and molecular biology. A survey of X-ray investigations performed with synchrotron radiation

may be found in the last section of the article by Gudat and Kunz [18].

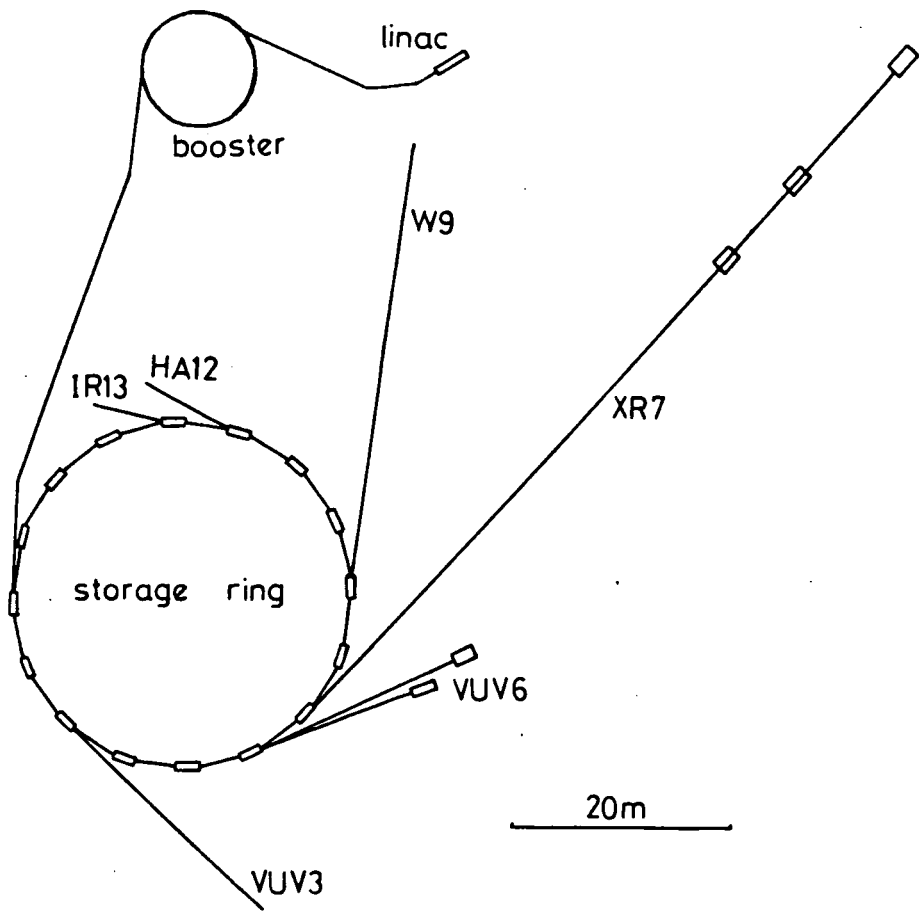


Figure 1.5: Schematic view of Daresbury Laboratory SRS.

Figure 1.5 shows schematically the geometry of the storage ring source (SRS) at SERC's Daresbury Laboratory. Electrons are injected from a 10 MeV linear accelerator and accelerated in a 600 MeV booster synchrotron. An intense beam is then built up in the main ring by continued injection from the booster. The electrons travel in an evacuated tube and are held in a circular orbit by a 31 m

diameter ring of electromagnets. After being slowly accelerated up to a full energy of 1.8 or 2.0 GeV they are stored for several hours while the synchrotron radiation is used in experiments. The long (80 m) X-ray beam line is designed to give good resolution for topography.

The radiation is concentrated in a narrow cone tangential to the ring, has a continuous spectrum extending from the microwave to the X-ray region, and is strongly polarized in the horizontal plane. It appears as a regular sequence of pulses whose frequency is determined by the number of electron bunches in the ring, the ring dimensions, and the electron velocity. Under normal operating conditions the SRS has 160 electron bunches stored and this emits a 200 ps width pulse every 2 ns. In single bunch operation such a pulse (see Figure 1.6) is emitted only once every 320 ns. The wiggler enhances the intensity in the hard X-ray region - at wavelengths below 1 Å - by using superconducting magnets to curve the electron beam very sharply in its vicinity. Figure 1.7 shows the spectrum of synchrotron radiation with and without the wiggler.

Synchrotron white beam X-ray topography was first performed by Tuomi et al [19] in 1974 and is now a well-established technique. Because the source is a white beam rather than characteristic radiation, the technique used is the Schulz method [20] which was originally developed by Guinier and Tennevin [21]. Since the source and the beam

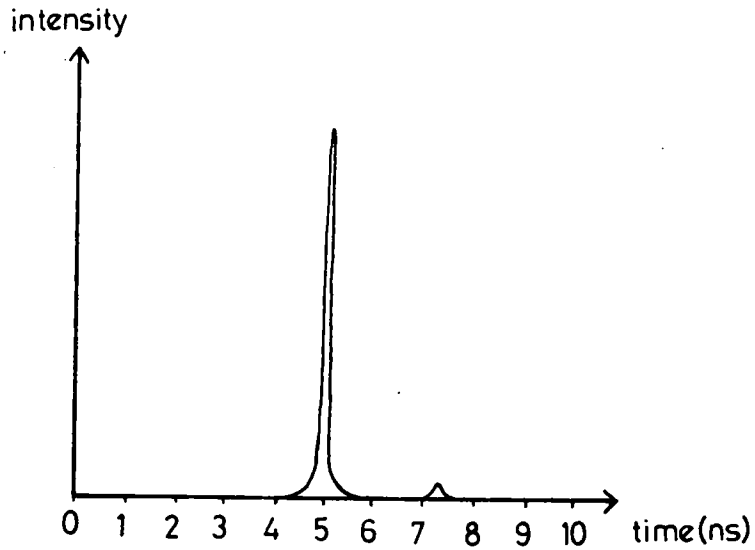


Figure 1.6: Structure of a pulse of synchrotron radiation from the SRS.

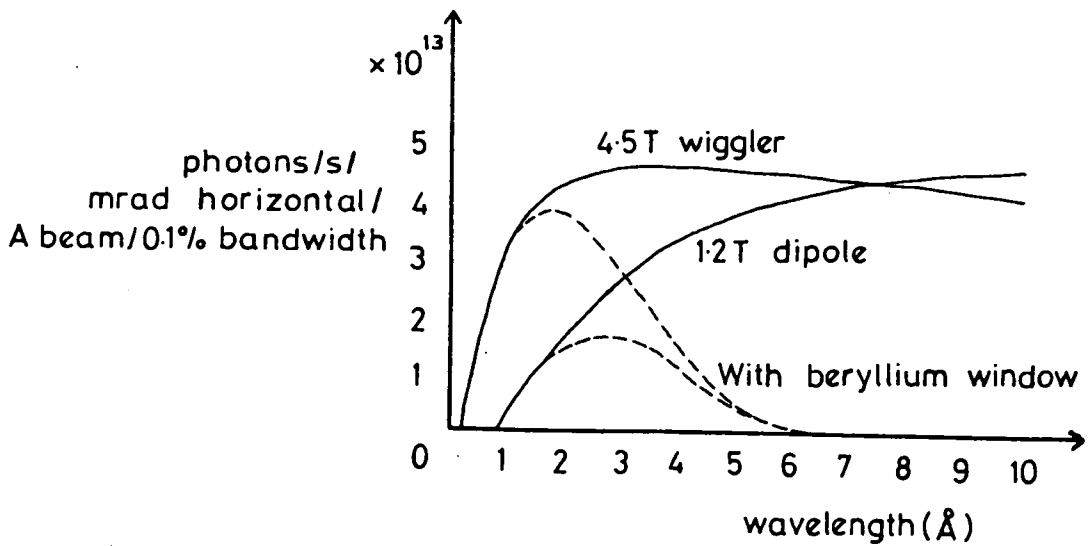


Figure 1.7: Spectrum of synchrotron radiation from the SRS with and without the wiggler.

divergence are both small, a single crystal placed in the beam produces a Laue pattern of "spots" as in the laboratory except that due to the high resolution each spot contains an image of the crystal similar to those obtained using the laboratory based Lang method. The broad beam falls on the crystal and the detector is set normal to the desired diffracted beam, as illustrated in Figure 1.8. Exposure times are much shorter than the corresponding laboratory times, partly because of the increased beam intensity and partly because scanning is not required.

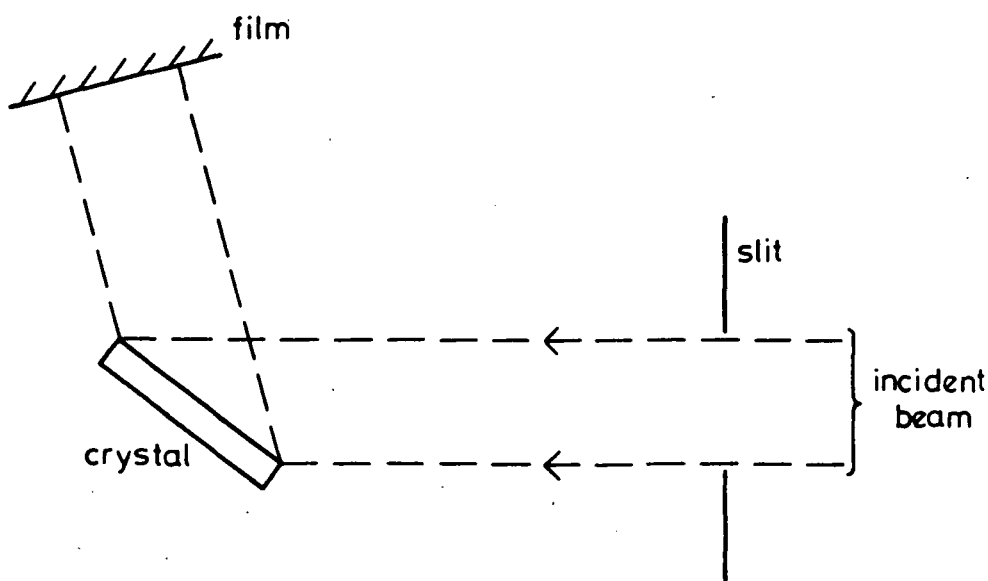


Figure 1.8: Experimental geometry for synchrotron radiation white beam reflection topography.

It is important to pay attention to signal-to-noise problems in almost any synchrotron radiation work, especially with white beams. General fluorescence and air scattering are far more troublesome than with conventional

generators, where the continuous background is quite low. Slits and shutters should be made out of Pb-Fe-Al sandwiches so that penetrating radiation is replaced by soft radiation, which is air-absorbed. The best material to use for specimen supports is plastic.

Precautions must also be taken to ensure that the Laue spots do not superimpose. For a given cross-sectional area of crystal this imposes a minimum distance between sample and detector, possibly at the expense of resolution. Several topographs may be taken at once using different diffracted beams. In this case only those spots with comparable recorded intensities may be handled simultaneously if similar image qualities are sought. Geometrical image distortion may also reduce the number of usable images.

1.3 Stroboscopy

Stroboscopic experiments have been used extensively for visible light microscopy of periodic phenomena such as magnetic domain wall motion, but only recently have such techniques been applied to X-ray diffraction topography. The main reason for this is that X-ray fluxes from conventional generators are extremely low compared with those from visible light sources. X-ray topographs taken with conventional generators take typically several hours

or more to record on the Nuclear Emulsion plates used for high resolution work and conventional beam-chopped stroboscopic methods raise this to totally unacceptable levels. However, with the establishment of synchrotron radiation facilities, exposure times for X-ray topographs have dropped from many hours to several minutes. A clear analysis of the relative fluxes available from synchrotron radiation and conventional sources has been given by Bonse [22].

Miltat and Kleman [23] have reported successful beam-chopped stroboscopic X-ray topography experiments in which the non-equilibrium positions of magnetic domain walls in Fe-3.5%Si were studied under a low-frequency driving field which was phase-locked to the mechanical chopper drive. Under the action of a sinusoidal applied magnetic field, oscillations of both 180° and 90° domain walls were observed. Sequences of topographs were recorded for a series of different phase relationships between field and chopper. Interactions between the walls and precipitates or dislocations were observed. These were indicated by the broadening of the images of some 90° walls due to localized instabilities. Although the details are not yet understood, the interaction is thought to imply nucleation and collapse of tiny closure domains. These defect-induced instabilities are exceptional; in general the observation of wall images as narrow as in the static situation implies a remarkably stable periodicity of the displacements. A review of some

possible beam-chopping methods for low-frequency stroboscopy has been given by Hart [24].

However, for high frequency experiments it is much more efficient to exploit the time structure of the synchrotron radiation itself; provided that certain discrete frequencies of operation can be tolerated, the whole of the available flux can be used. At Daresbury Laboratory SRS, if a periodic exciting signal can be phase locked to the synchrotron radiation emission, stroboscopic experiments at multiples of 3.122 MHz can be performed. The time resolution is excellent as the mark-space ratio at 3.122 MHz is 1:1600.

The key to stroboscopic topography is the exact synchronization of the observed phenomenon to the time structure of the source. The latter is defined by a master oscillator which controls the rf cavities of the storage ring. A square wave signal obtained from this oscillator is frequency multiplied and filtered to produce a sinusoidal signal of the same frequency as that of the phenomenon of interest. Amplification then produces a driving signal which is ideal for application to stroboscopy since it is phase-locked to the synchrotron radiation emission. Goddard et al [25] have described the instrumentation and experimental requirements for stroboscopic investigations. These are illustrated schematically in Figure 1.9. The periodic strains are usually imaged using white radiation reflection topography. The strains associated with

different instants in the cycle can be examined by inserting a time delay into the driving signal line.

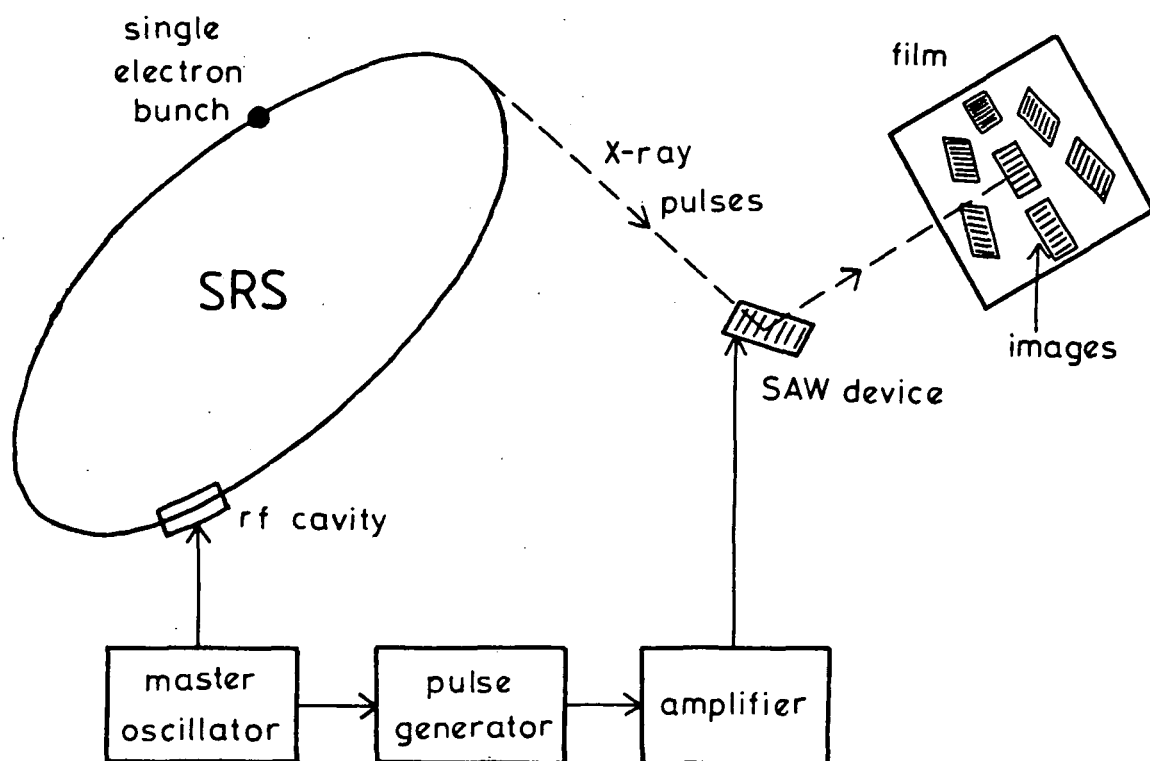


Figure 1.9: Schematic diagram of the experimental arrangement for stroboscopic topography using the time structure of synchrotron radiation.

Stroboscopic topography using the time structure of synchrotron radiation may be used to investigate devices which operate in the MHz region. Gluer et al [26] first demonstrated the feasibility of the technique by studying standing bulk waves and their effect on the image formation of dislocations in AT-cut quartz single crystals. For this

cut of crystal the dominating vibration mode is the thickness shear mode - a standing transverse wave. Secondary modes were suppressed because of the shape of the crystal. The crystal was designed to resonate at the same frequency as the synchrotron radiation from the storage ring DORIS. Their experiments were performed at the white beam topography station at HASYLAB [27]. The sample was mounted inside a vacuum chamber in order to lower the background radiation caused by air scattering, and the film was placed outside the chamber behind a lucite window.

A series of projection topographs showed that around a zero-crossover of the acoustic vibration faint secondary modes were visible which could never be seen by continuous exposure. Slight motions of and contrast changes of the dislocation images were observed.

Section topographs showed clearly the areas with maximum curvature of the planes. There was also a surprisingly strong contrast change of dislocation images. The direct images moved at a speed equivalent to a few times the velocity of sound in quartz, these movements being insensitive to the sign of the strain. There is, as yet, no straightforward explanation for the motion of the dislocation images. However, a reasonable correspondence of calculated and observed image positions is obtained if the intersection of the dislocation line with the opposite boundary of the Borrmann triangle is identified as the source of the image. This phenomenon requires further

analysis.

All subsequent work has concentrated on studies of surface acoustic wave devices. The devices are described in Chapter 2, and the stroboscopic topography investigations are discussed in Chapter 3.

CHAPTER 2: SURFACE ACOUSTIC WAVE DEVICES

The surface acoustic wave (SAW) device has played an important part in modern radar systems for a number of years and is now a standard component in consumer TV sets and video games as an intermediate frequency (IF) filter. Its design is based on the generation and detection of surface acoustic waves.

2.1 Surface Acoustic Waves

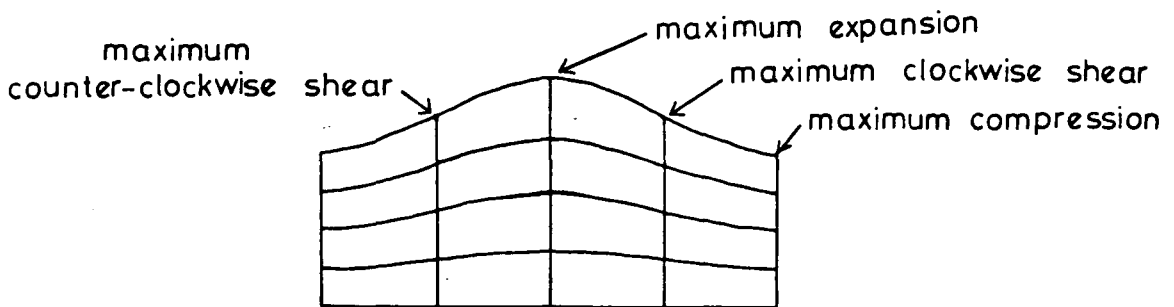


Figure 2.1: The features of a surface acoustic wave.

Surface acoustic waves [28] are analogous to surface waves on water and are manifested as a mechanical disturbance on the surface of an elastic material. These Rayleigh waves are two-dimensional, having a longitudinal component in the direction of propagation coupled to a

transverse component perpendicular to the surface. At the surface the particle motion is elliptical and retrograde; deeper in the substrate the sense of circulation changes. Both the longitudinal and transverse components attenuate rapidly with depth so that most of the acoustical energy is confined to a layer about one wavelength thick (see Figure 2.1).

Elastic waves in a charge-free piezoelectric solid can be described using the linear theory of elasticity [29]. The waves are found by solving a system of four coupled wave equations for the three elastic displacements u_j and the electric potential ϕ_E . At large depth in the crystal u_j and ϕ_E should vanish. At the surface, the potential should be continuous and fulfil Laplace's equation outside the crystal. Usually the solution for a SAW is written as a linear combination of partial waves:

$$u_j = \{ \sum C^{(n)} \alpha_j^{(n)} \exp(iKb^{(n)}x_3) \} \exp[iK(x_1 - vt)]$$

$$\phi_E = \{ \sum C^{(n)} \alpha_4^{(n)} \exp(iKb^{(n)}x_3) \} \exp[iK(x_1 - vt)]$$

j=1,2,3 (2.1)

where K is the acoustic wave number, v the phase velocity, $C^{(n)}$ the weighting coefficients, $\alpha_j^{(n)}$ the amplitudes and $b^{(n)}$ the decay constants of the partial waves, x_1 is the direction of wave motion, x_2 is perpendicular to x_1 in the surface plane, and x_3 is perpendicular to the surface.

2.2 Materials

Based on the use of piezoelectric materials, SAW devices do not generally place too stringent a requirement on crystal perfection. However, the range of materials which are suitable is small and these do not offer a wide spectrum of frequencies of operation.

If there is one single most important characteristic of a crystal resonator it is its behaviour with respect to temperature. All other design criteria usually have to be resolved with the constraints of the desired temperature characteristic superimposed. For frequency control applications, the lowest possible dependence of the relevant resonator properties on temperature is essential.

Quartz is used extensively in device applications because it has good temperature stability which makes it popular for large devices and for military operating conditions, and a rather small electromechanical coupling factor which makes it almost ideally suited for application to frequency control and selection. Lithium niobate, LiNbO_3 , is another commonly used material [30]. It equals quartz in chemical and physical stability, surpasses it in terms of Q, but presents problems in simultaneously meeting temperature coefficient and mode purity requirements. However, because it has a large coupling coefficient it is attractive for use in broad-bandwidth devices such as IF and reflective array compressive filters [31].

Neither material is ideal but no other material has been grown with sufficient quality in the sizes and quantities required to offer a serious alternative. A large number of materials have been examined for their possible applications as SAW substrates [32]. Berlinite [33] and lead potassium niobate [34] are promising in terms of their temperature coefficients but present severe crystal growth problems. Recently, work has been performed [35] on lithium tetraborate, $\text{Li}_2\text{B}_4\text{O}_7$, to assess it for SAW applications. XZ- $\text{Li}_2\text{B}_4\text{O}_7$ is temperature-compensated and so could offer a viable future alternative to quartz and lithium niobate. This is discussed further in Chapter 5.

Material	Crystal Cut and Orientation	Piezoelectric Coupling Const. k^2 (%)	Acoustic velocity v (ms^{-1})	Delay time temp. coefft. ($\text{ppm}/\text{C}^\circ$)
LiNbO_3	YZ	114.5	3488	91
$\text{Bi}_{12}\text{GeO}_{20}$	(111), (011)	1.7	1680	128
ZnO	basal	1.0	2700	40
LiTaO_3	YZ	0.74	3200	37
Quartz	YX	0.23	3170	-22
Quartz	ST, X	0.16	3150	0
$\text{Li}_2\text{B}_4\text{O}_7$	XZ	1.2	3510	parabolic

Table 2.1: Physical constants of typical SAW materials.

In general, the coupling efficiency between a Rayleigh wave and surface electrodes is largest for materials with high piezoelectric coupling constants. For a given

piezoelectric crystal it is important to know the surface orientations and propagation directions for which most efficient conversion is possible. The key crystal parameters for SAW devices are given in Table 2.1 for typical materials and crystal orientations.

2.3 Devices

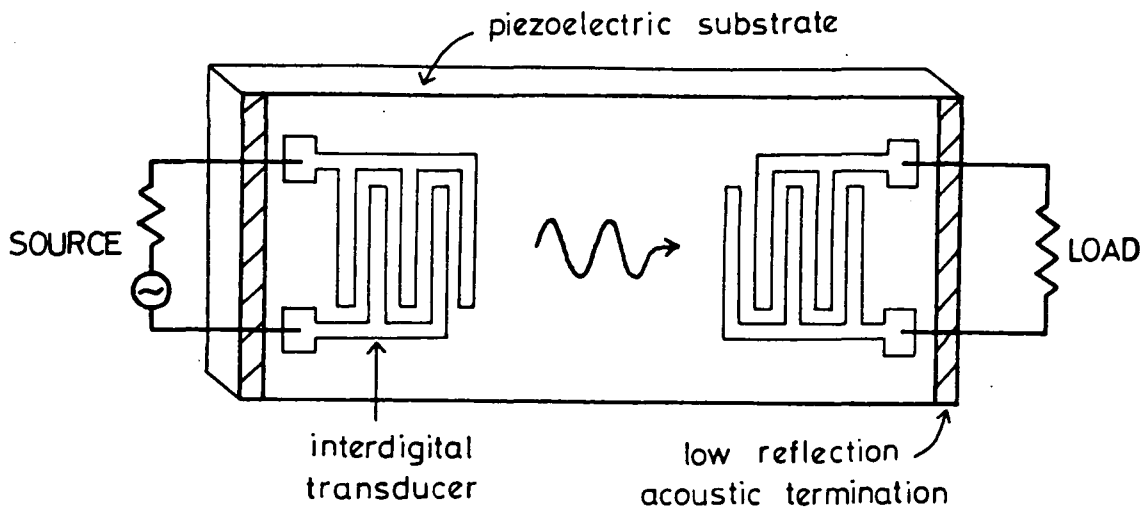


Figure 2.2: Schematic diagram of a SAW delay line.

The basic operation of a SAW device can be seen from Figure 2.2 which represents schematically the layout of such devices. By means of an interdigital transducer (IDT) electromagnetic signals generate surface waves due to the inverse piezoelectric effect. The most simple and efficient transducer consists of an array of conductive electrodes

vacuum deposited on the surface of the piezoelectric substrate. When an external rf voltage is applied between the two interleaved comb-shaped electrodes an electric field is generated which produces local stresses in the medium; this launches a surface acoustic wave which travels in both directions along the substrate. The wave travels with relatively low loss and can be converted back into an electromagnetic wave by means of a second similar transducer; this is possible because the transducer operation is reversible - a time-varying output voltage results from the contributions of the instantaneous electric fields associated with the elastic wave propagating under the electrodes. This procedure has two advantages. Firstly, because the velocity of the acoustic wave is typically 10^{-3} ms^{-1} , delays in signals can be generated much more conveniently than using purely electromagnetic means. More importantly, perhaps, as the signal is travelling along the surface of the material it can be accessed and a variety of signal processing functions can be performed. Such SAW devices are analogue signal processing devices, useful in the frequency range from a few MHz to 2000 MHz.

An important property of the devices is that there is a one-to-one relationship between the transducer geometry and its impulse response, the overlap of the electrodes determining the amplitude, and the position of the electrodes determining the phase. Thus the phase and

amplitude of a signal can be determined separately by the geometry of the transducers.

In regions without overlap, adjacent electrodes have the same polarity and no electric field exists. An acoustic wave is generated only in so-called active regions where adjacent electrodes of opposite polarity overlap. Diffraction spreading is larger for waves from electrodes with small overlap, but the effect is minimal in self-focussing substrates like LiNbO_3 .

Reflections between transducers are eliminated by the use of double finger IDT's or by the use of two output transducers staggered in position by $\lambda/4$, where λ is the acoustic wavelength. The reflections from these cancel at the centre frequency.

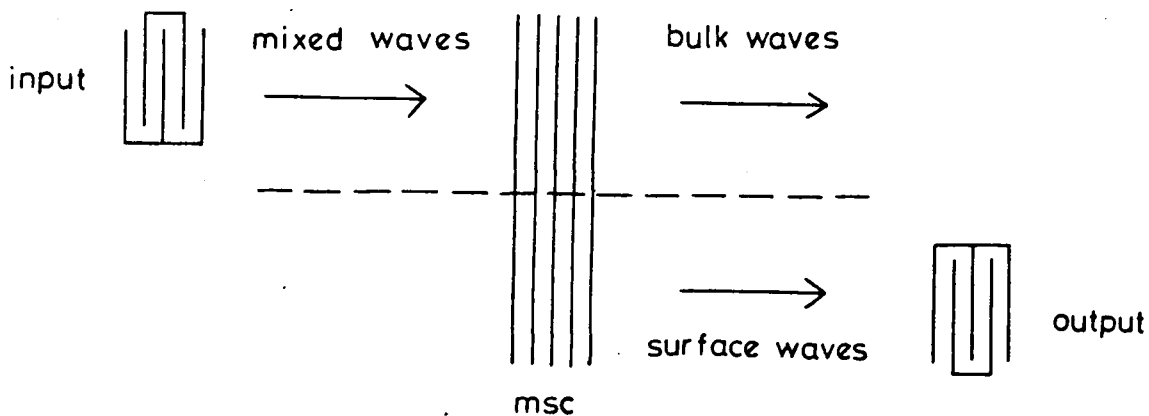


Figure 2.3: Schematic view of a multistrip coupler with input and output IDT's.

In high performance SAW TV-IF filters, multistrip

couplers [36] are used to suppress unwanted spurious bulk mode transmission. The multistrip coupler (msc) may be considered schematically as in Figure 2.3. It consists of an array of parallel metallic strips positioned transverse to the direction of propagation on the piezoelectric substrate. If an acoustic surface wave is launched into one half of the structure, alternating potential differences are set up between adjacent metal strips. These potentials must also appear in the other track where they generate a new acoustic wave. When a multistrip coupler is used the surface waves are coupled across to be received by the second transducer while the bulk waves continue on their original path [37]; thus the multistrip coupler can be used to discriminate between surface waves and bulk waves. It can be shown [38] that there is total transfer of the surface waves from one track to the other when the phase difference between the tracks is $\phi = \pi/2$.

A wide variety of functions are possible with SAW devices. The simple delay lines can provide delays of up to 20 μs but tend to be used in applications requiring shorter delays. The basic delay element is also used in the SAW oscillator. In these devices the output is fed back to the input after suitable amplification. Frequencies which satisfy the condition that the phase shift round the loop is $2\pi N$ are thereby generated. By suitable choice of the transducer geometry, one frequency can be selected and effective stable oscillations in the frequency range 100-

200 MHz can be made. This range is higher than that available with bulk wave devices and has the advantage that, according to the design, stability can be traded against an ability to modulate the frequency over a range of a few per cent.

Filtering is perhaps the most important application of SAW devices; very complicated impulse responses can be implemented simply by varying the position and overlap of the electrodes. A variety of spatial signal processors such as Fourier transformers, convolvers and correlators are also possible.

There is a great variation in size. Some devices, such as those required for television, are quite small and are comparable to the size of silicon integrated circuits. Others, particularly the pulse compression filters, can be as large as 25 cm in length.

It is important that power is not lost from the devices. As the device design is being improved there is concern about the quality of the substrates. Subgrain boundaries and groups of dislocations scatter the primary wave into either other unwanted surface waves or into bulk waves. Substrates such as LiNbO_3 may also contain surface defects known as rilles - regions of reverse polarization which remain after the polling process. It is well known that devices which contain many rilles do not perform well. As with other devices which are made in large volumes, the uniformity of crystal parameters over large wafers is

essential. This calls for greater control over the basic substrate quality; X-ray topography is a valuable tool for this purpose.

2.4 Methods Of Detection

Standing vibrational mode patterns have been investigated using many techniques; some of these have been reviewed by Spencer [39]. Recent techniques include the application of holography to the study of surface waves [40] and the use of the scanning electron microscope to obtain vibrational patterns [41]. None of these, however, can match the power of X-ray topography [42] to examine the displacements.

On the other hand, the investigation of travelling waves by conventional topography can give no information about the periodic nature of the strains. However, conventional topography has been applied [43] to the imaging of the average strain fields associated with propagating SAW's. The generation of standing waves does of course permit imaging of the periodicity using this technique although it gives information of limited relevance since most devices operate by propagating travelling waves. Techniques exploiting electrostatic [44] or optical [45] probes can be used to detect the electric fields or mechanical displacements associated with a

propagating SAW but they give no information concerning crystallographic lattice strains or bulk defects. Similarly, the scanning electron microscope working in the stroboscopic voltage contrast mode has been used [46] to study travelling Rayleigh waves on piezoelectric substrates, but only surface defects and charges can be imaged in this way.

However, stroboscopic X-ray topography can be used [47,48] to image the strain fields associated with propagating SAW's together with static crystallographic defects such as dislocations and low angle grain boundaries. This makes it a valuable tool in the development of devices based on the generation and detection of such waves.

CHAPTER 3: STROBOSCOPIC TOPOGRAPHY OF SURFACE ACOUSTIC WAVE DEVICES

3.1 Investigations of Surface Wave Devices

Whatmore et al [47] first made use of stroboscopic topography to image travelling surface acoustic waves on a Y-cut Z-propagating 38 MHz LiNbO_3 television IF filter (Appendix A gives a diagram of this crystal cut). They have demonstrated that the technique has considerable potential as a diagnostic tool for SAW device technology. Interactions between the Rayleigh waves and microscopic crystalline defects were observed which provide new insights into the factors affecting SAW device performance. Their experiments were performed using the white beam topography station [49] at Daresbury Laboratory SRS. An X-ray topograph taken without synchronization of the illumination and the driving signal showed only the standing waves excited within the transducer. The electrodes of the transducer are not visible on topographs. With the driving signal phase-locked to the synchrotron radiation emission, a periodic array of light and dark bands was visible, successive dark bands corresponding to one wavelength of the travelling wave. By recording topographs at different instants in the cycle, a periodically occurring interaction was observed. This could not have been detected other than by stroboscopic

methods. Other interactions were observed which were present throughout the cycle.

The defects which cause these interactions have been investigated [48]. Rilles, which were visible as depressions under Nomarski interference contrast microscopy after chemical etching, were correlated with subgrain boundaries. From recorded topographs, microdensitometer scans were made parallel to the wavefronts on both sides of such a defect. The scans showed that considerable disruption to the wavefront uniformity was caused by the defect. A scan made perpendicular to the wavefronts revealed a marked reduction in energy in the wave. This indicates an interaction between the wave and the defect by which energy is scattered from the defect. Whether this is associated with the rille or the subgrain boundary or a combination of the two has yet to be determined.

Microdensitometer scans also demonstrated the reduction in intensity of the primary wave in the multistrip coupler accompanied by a growth of the secondary wave. This corresponds to the transfer of energy across the multistrip coupler. Examination of the topograph revealed the predicted phase shift of $\pi/2$ in the acoustic wave along the multistrip coupler.

Successful experiments have also been performed [50] on other LiNbO_3 devices and on quartz devices operating at 62.44 MHz. However, experiments at frequencies of 500 MHz [48] have been unable to detect discrete wavefronts because

of the limits on resolution. Nevertheless, future double crystal experiments could make wavefront imaging possible at these technically important frequencies.

3.2 Mechanism of Image Contrast

Although advances had been made in the application of stroboscopic topography to the examination of SAW devices, it was not until recently that the mechanism of contrast was understood. It had been expected [50] that the contrast mode was one of extinction contrast - due to the properties of the continuous X-ray spectrum, regions of strain show up always as regions of increased intensity irrespective of the sign of the strain. Thus a pattern of wavefronts separated by half an acoustic wavelength was expected in the image. This was not observed; successive dark lines corresponded to one wavelength of the travelling wave.

Cerva and Graeff [51,52] have explained the origin of the SAW contrast by showing that close to the crystal a contrast dominates which does have the expected half wavelength separation of the wavefronts and which arises from X-rays passing through a fairly thick bulk layer. However, far from the crystal the major part of the contrast is orientation contrast of the curved planes, and so the wavefronts are separated by one acoustic wavelength.

3.2.1 Orientation Contrast

The orientation contrast can be explained because the extinction distance is usually small compared to the acoustic wavelength; thus the curvature of the planes changes only slightly over the extinction distance. It is then possible to approximate the reflection by a simple mirror reflection from a corrugated surface, although this neglects the changing lattice orientation seen by a penetrating wavefield. The orientation contrast can then be investigated by ray tracing calculations. By defining an appropriate co-ordinate system, as shown in Figure 3.1, Cerva and Graeff [51] were able to determine the film co-ordinates, x_f and y_f , in terms of the incidence parameters:

$$\begin{aligned}x_f &= (L+D)\phi + 2Da_t K \sin\phi \sin\theta \sin\beta \\y_f &= (L+D)\psi + 2Da_t K \sin\phi \cos\beta\end{aligned}\tag{3.1}$$

where L = source-specimen distance

D = specimen-film distance

a_t = transverse amplitude of the acoustic wave

ϕ, ψ are angles expressing the angular deviation of the incident beam

θ = angle between the incident ray and the crystal surface

β = angle between the diffraction plane and the propagation direction

and $D = \frac{r_c \cdot K}{\sin\theta}$ with $\underline{r_c} = (x, y)$ a point on the unperturbed crystal surface
 $= LK(\phi \sin\beta - \psi \cos\beta / \sin\theta)$

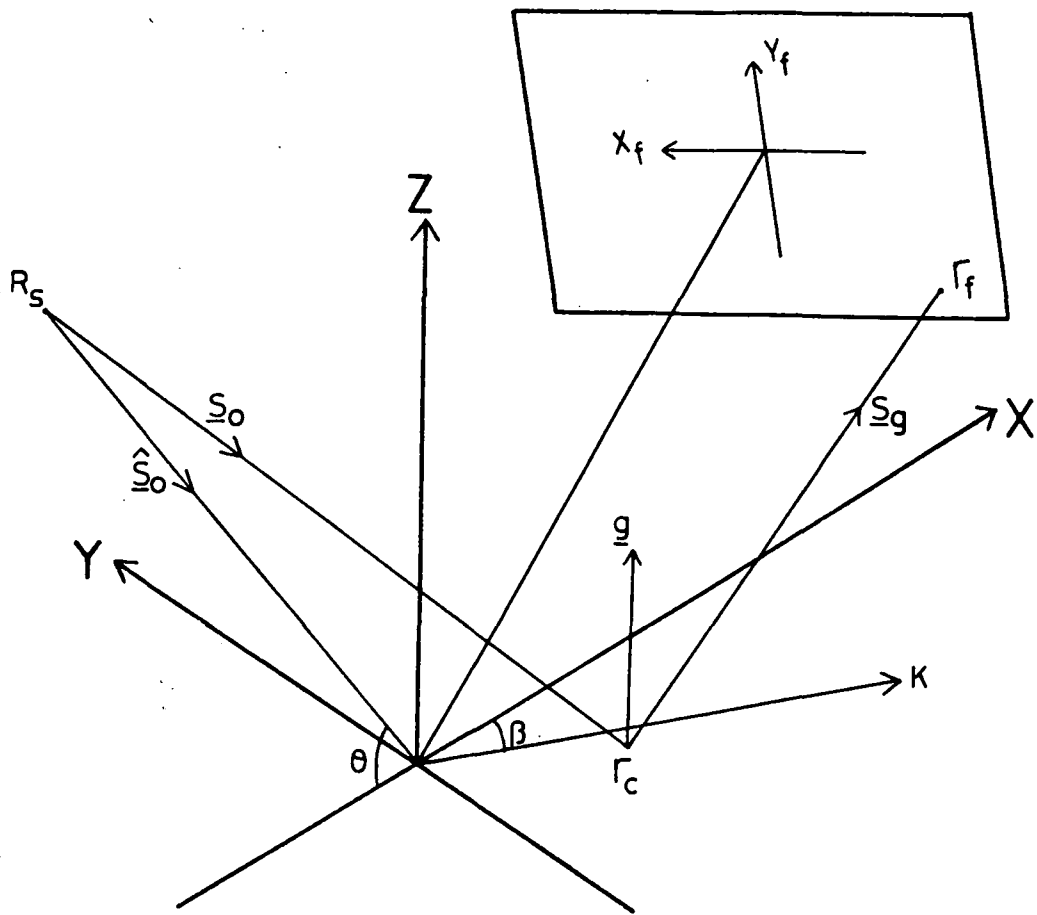


Figure 3.1: Co-ordinate systems used to simulate orientation contrast.

By using equation (3.1) they have produced ray tracing maps for different crystal to film distances. These show that the troughs of the surface wave focus the reflected waves at a certain distance whereas the crests defocus the waves; this results in a non-sinusoidal pattern in the image with a periodicity of one acoustic wavelength.

With the use of equation (3.1), an expression for the

dependence of the local intensity on the incidence parameters has also been derived:

$$I/I_0 = [1 + 2Da_t K^2 \cos\Phi (\sin\theta \sin^2\beta + \cos^2\beta / \sin\theta) L / (L+D)]^{-1} \quad (3.2)$$

Beyond a certain specimen-film distance $D=D_F$, the focal distance, there are several contributions to the intensity in certain areas and these must be added together.

The application of the linear theory of elasticity to the SAW waves leads to an expression for the amplitude of the waves:

$$a_t = 1/2 (c_3 G(\omega) / \omega a)^{1/2} V_{in} \quad (3.3)$$

where c_3 = elastic constant = $6.86 \times 10^{-12} \text{ m}^3 \text{ J}^{-1}$

ω = frequency of SAW

$G(\omega)$ = input conductance

a = aperture of IDT

and V_{in} = peak applied voltage

If this calculated wave amplitude is inserted into equation (3.2) then a theoretical variation of intensity with input voltage can be obtained. Comparison with experimentally obtained intensities gives satisfactory agreement.

An expression for the focal distance D_F was also obtained from equation (3.2):

$$D_F = \sin\theta [2a_t K^2 (\sin^2\theta \sin^2\beta + \cos^2\beta)]^{-1} \quad (3.4)$$

This indicates that for a given amplitude a wave travelling oblique to the scattering plane gives weaker contrast than one with a parallel direction.

By finding the focal distance D_F and measuring the

acoustic wavelength and incidence parameters, the acoustic amplitude can be determined using equation (3.4). Unfortunately, a source size of a few tenths of a millimetre is required to measure the focal distance. A small pinhole close to the source is necessary to obtain sufficient accuracy.

Experiments to demonstrate the theory were performed using Y-cut Z-propagating LiNbO_3 devices having only one IDT (see Appendix A). The substrate had no grain boundaries or ferroelectric domains to impair wave propagation. Topographs were taken using reflection from the surface planes. A topograph was taken with no excitation of the surface waves; distortions in the area where the crystal was fixed to the mounting gave a strong orientation contrast. When surface waves were excited, orientation contrast was again observed best where the waves passed the distorted area of the surface; this could be seen because the spacing of the image wavefronts was broadened or narrowed depending on the sense of curvature of the planes.

The contrast formation of the SAW was demonstrated by placing in front of the crystal a thin wire inclined to the wave propagation direction. The wire gave rise to two shadows - one formed by the incident beam and the other by the reflected beam. The borders of the latter are wavy but sharp; the wavy shape is caused by the troughs focussing the waves while the crests defocus them. On the other hand, the shadow formed by the incident beam has diffuse image

borders which arise from additional contrast formed by wavefields which penetrate into the bulk of the crystal. Thus intensity is detected from an area not originally illuminated.

3.2.2 Wavefield Deviation Contrast

Cerva and Graeff [52] have shown that this additional contrast can be related to the deviation of X-ray beams in the deformation field of the acoustic wave. This contribution can be separated from the surface reflected waves by using narrow entrance slits. They have calculated the beam paths inside the crystal and the intensity profiles at the surface. The intensity has two nearly equal peaks within one acoustic wavelength. However, when the specimen-film distance is increased this contrast changes to orientation contrast with only one peak per wavelength.

Owing to its geometrical origin, orientation contrast is wavelength independent. However, this is not true for the additional contrast. Therefore Cerva and Graeff tried to optimize the contribution to the intensity from the (0660) reflection in their experiments. This was achieved by tuning the wavelength of the (0990) reflection so that it was below the Nb K-absorption edge. Thus the (0330) and (0990) contributions were strongly suppressed by absorption.

The additional contrast was convincingly demonstrated by collimating the incident beam with a 10 μm slit. The diffraction geometry was chosen such that the acoustic wavevector and the slit blades were perpendicular to the diffraction plane. An accurate position of the slit relative to the acoustic wave was obtained by first taking a topograph with the whole sample illuminated and then exposing the same topograph with the slit intersecting the beam.

Another topograph was taken with the slit in place. This showed spots of higher intensity marking wave troughs alternating with areas of lower intensity marking wave crests. This part of the image is caused by orientation contrast. However they also observed intensity spikes at one side normal to the slit image. Since this region was not illuminated, they assumed that wavefields which penetrated into the bulk of the crystal were deviated by the strain field of the SAW and emerged at the entrance surface. These wavefields reach the surface at the locations of wave troughs only; in the regions of wave crests no enhanced intensity is recorded.

A topograph was taken with the sample rotated about its surface normal so that the acoustic wavevector was lying in the diffraction plane. The deviated intensity in the region of the SAW propagation was clearly observed. The change in the deviated intensity pattern at different phases of the acoustic waves has also been shown.

The explanation of these observations requires the application of the theory of wave propagation in slightly deformed crystals [53]. This depends on the incident beam being made up of monochromatic plane waves. Fortunately, for white synchrotron radiation the large source-specimen distance allows us to consider an incident wave as nearly plane. However, because the wavelength changes, the white beam has to be considered as a monochromatic beam with large divergence which excites the dispersion surface incoherently.

By using this theory, Cerva and Graeff [52] were able to show examples of calculated ray paths and corresponding intensity distributions. Many independent wavefield paths are formed inside the crystal. Those waves which reach the surface give rise to deviated intensity which is calculated from the boundary conditions. The intensity distribution shows a large peak of surface reflected intensity at the entrance point. The penetrating wavefields are subjected to the strain field of the acoustic waves; two peaks of deviated intensity are formed which are separated by a distance which Cerva and Graeff have calculated to be about 70 μm . The calculated intensity distributions may be compared with topographs.

The calculation does not yield the direction of the deviated beams outside the crystal. That these beams are no longer parallel and hence show some orientation contrast similar to the surface reflected waves has been

demonstrated in an experiment where the slit was slightly tilted in relation to the surface and topographs were taken at different distances from the specimen. At a distance of 5 cm a series of ripples was seen where every alternate ripple was slightly more intense. The slight difference in intensity of the ripples is not caused by orientation contrast; it can be explained by the anomalous absorption phenomenon in Bragg reflection. For the wave troughs, the wavefields which are weakly absorbed are bent back to the surface whereas for the crests it is the more strongly absorbed wavefields which reach the surface. With increasing distance the more intense ripples become narrower and even more intense whereas the other ones are spread. Hence the orientation contrast dominates the intensity distribution at large distances.

It is evident that Cerva and Graeff [51,52] have made an elegant and thorough study of the contrast formation. They have shown that close to the crystal a contrast dominates which has peaks at both wave crests and troughs whereas far from the crystal orientation contrast dominates with peaks at the wave troughs only. These results will enable greater progress to be made in the study of SAW devices by stroboscopic topography, and the interaction of the acoustic waves with defects in the crystals can now be assessed in a more quantitative manner.

CHAPTER 4: EXPERIMENTAL INVESTIGATIONS OF SURFACE ACOUSTIC WAVE DEVICES

The technique of stroboscopic X-ray topography was outlined briefly in Chapter 1. This method was used to examine LiNbO_3 SAW devices and the propagation of Rayleigh waves along the surface. Lithium niobate has a trigonal crystallographic structure with space-group $R3c$, $a=5.147 \text{ \AA}$, and $c=13.856 \text{ \AA}$. The devices used for this work were LiNbO_3 television IF filters and were mainly Y-cut Z-propagating devices (see Appendix A).

4.1 Experimental Technique

The experiments described here were performed with Daresbury SRS running in single bunch mode at 1.8 GeV. 97% of the synchrotron radiation was concentrated in a single pulse of approximately 200 ps width at a frequency of 3.122 MHz. A square wave locked to this was obtained from the SRS ring monitors. This was frequency quadrupled using a pair of externally triggered pulse generators. The third harmonic of the fundamental was selected by passing the signal through an LC filter network. This signal was amplified to provide a 37.46 MHz sine wave signal capable of driving a 38 MHz LiNbO_3 television IF filter. Phase shifts were introduced into the driving signal simply by

adding standard lengths of co-axial cable between the power amplifier and the device. The experimental arrangement was as shown in Figure 4.1.

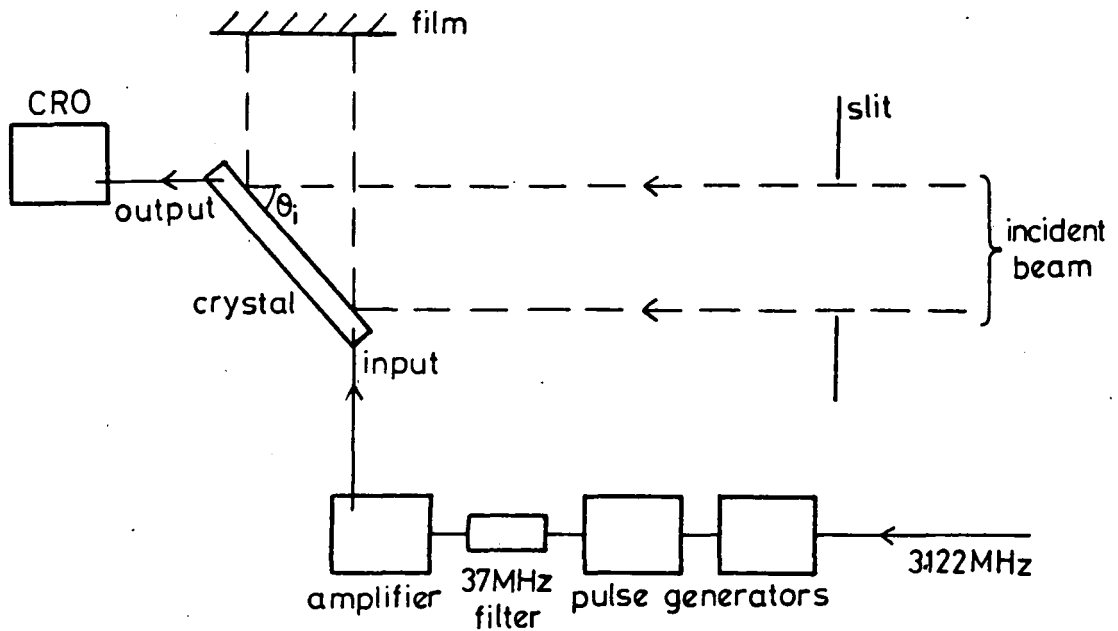


Figure 4.1: Experimental arrangement used to perform stroboscopic investigations.

White radiation topographs of the crystal were taken using the multipurpose diffractometer at the SRS topography station [49]. As the devices were mounted in standard T09 cans, great care was taken to illuminate only the specimen in order to avoid fluorescent emission from the brass. An aluminium and lead slit was constructed for this purpose. Despite image compression, topographs were recorded with the SAW propagating in the plane of incidence which was in the vertical. This was because the SRS source size is

smaller in the vertical direction and thus this setting gave best resolution of the wavefronts. The photographic material used was Ilford L4 Nuclear Emulsion plates of 25 μm thickness. The source-to-specimen distance was 80 m while the specimen to plate distance was varied between 35 mm and 65 mm. Exposure times were between 5 and 70 minutes.

4.2 Discussion of Experimental Results

Experiments were performed to investigate various aspects of SAW propagation. A computer program incorporating calculation of wavelengths, structure factors, and extinction distances has been written to simulate the diffraction pattern for LiNbO_3 with the incident beam at 45° to the the $(01\bar{1}0)$ surface planes. This has proved useful for identifying reflections and is given in Appendix B.

(a) Action of the Multistrip Coupler

An initial examination of six devices incorporating multistrip couplers was performed. These devices used 128° niobate (see Appendix A) and the transducer arrangement was as shown in the photomicrograph of Figure 4.2. Each device consists of an apodized and a uniform split-finger transducer with periodicities (λ_0) of 98 μm and apertures

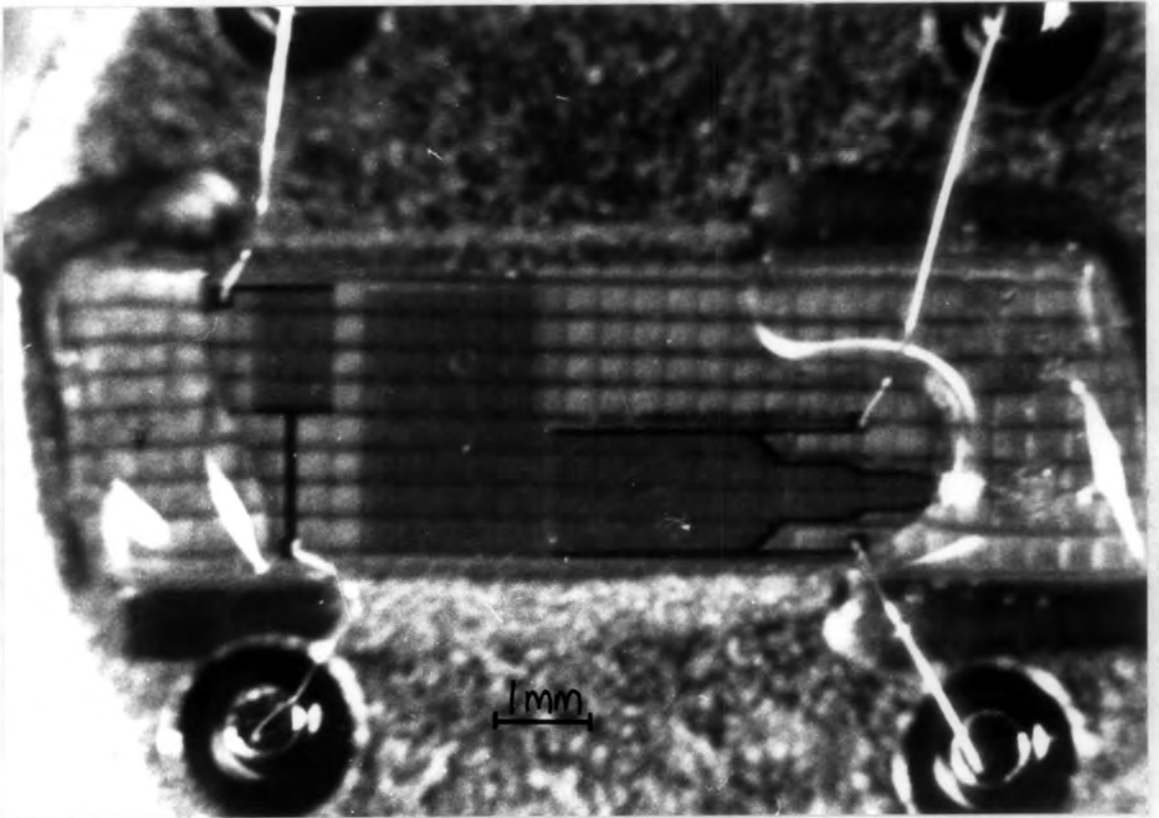


Figure 4.2: Photomicrograph of a SAW device incorporating uniform and apodized transducers and multistrip coupler.

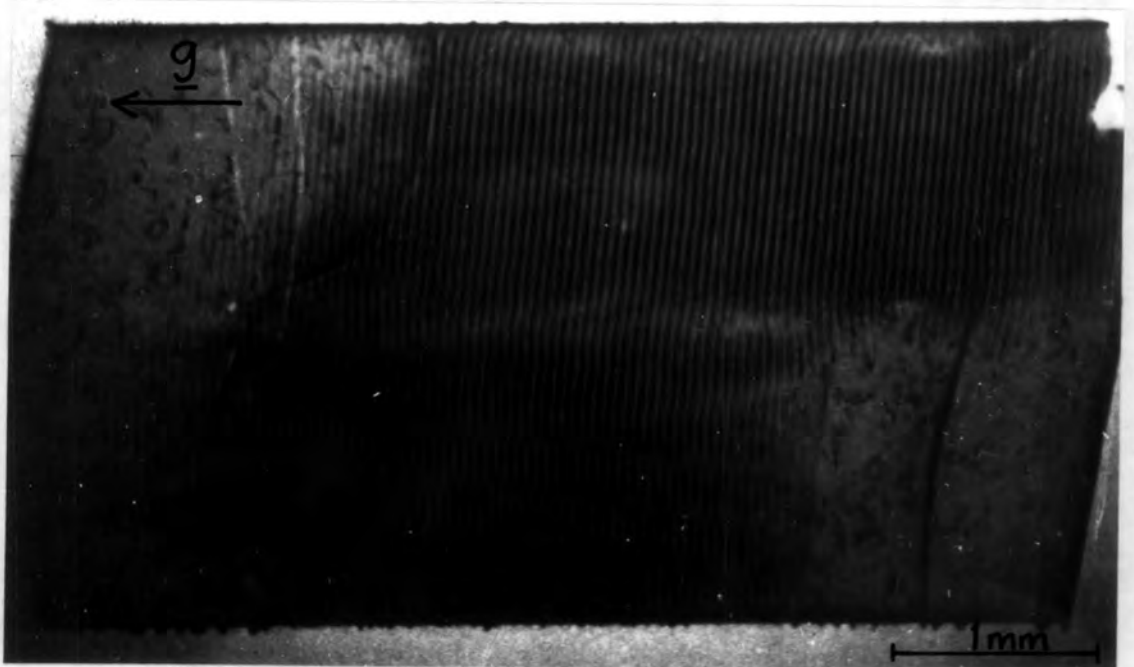


Figure 4.3: Stroboscopic X-ray topograph of device of Figure 4.2 with 15 V p/p input to uniform transducer.

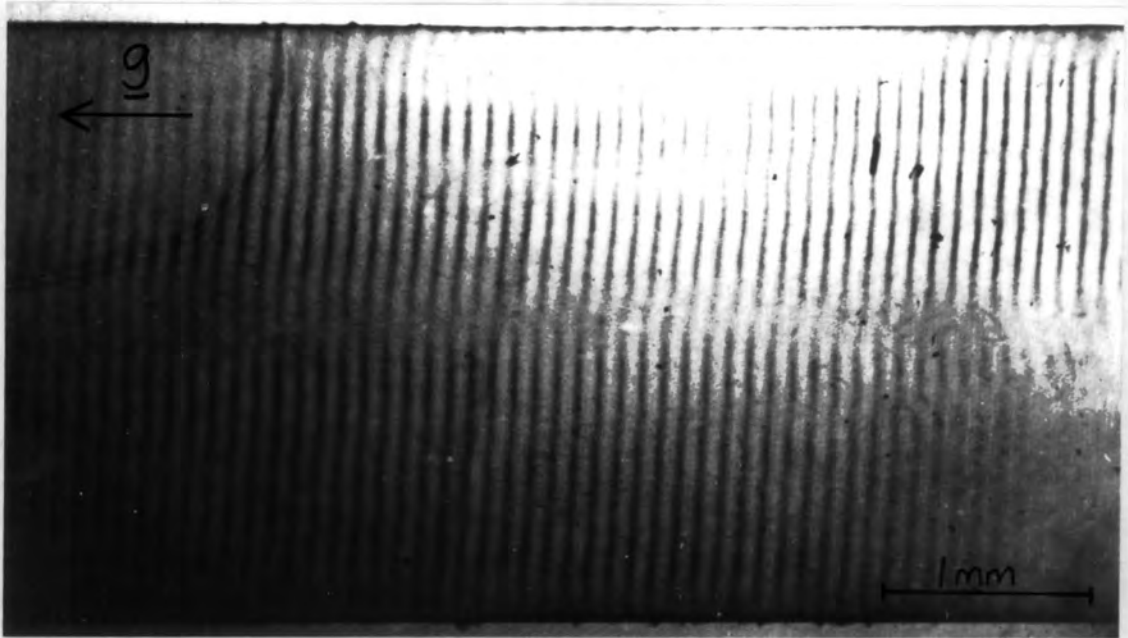


Figure 4.4: Detail of phase change of waves in multistrip coupler region of device of Figure 4.2.

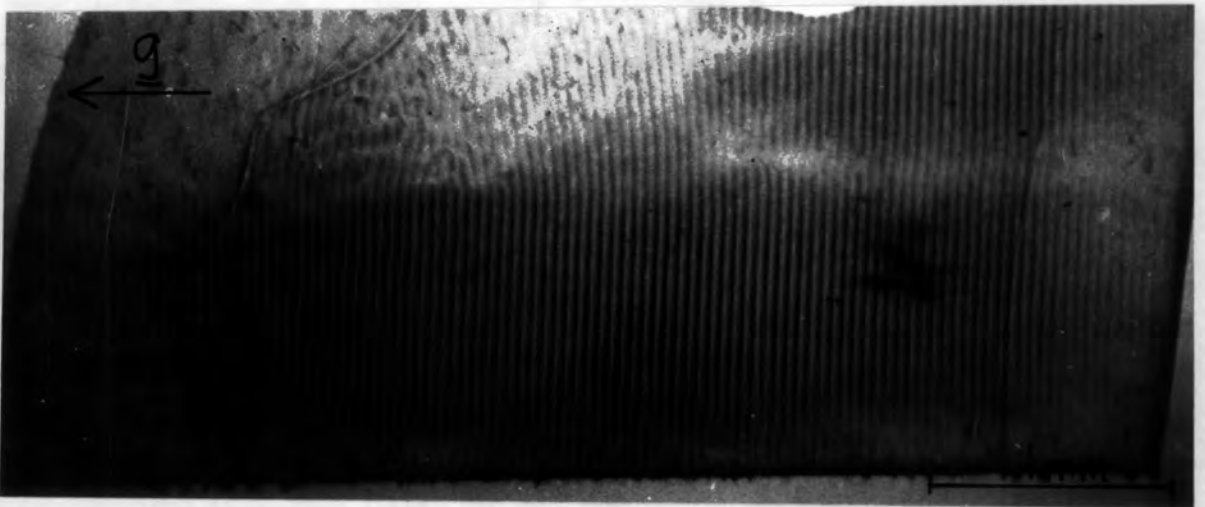


Figure 4.5: Part of device of Figure 4.2 with 15 V p/p input to apodized transducer.

of $20\lambda_0$, separated by a multistrip coupler of periodicity $49 \mu\text{m}$, width $40\lambda_0$ and length $26 \lambda_0$. This device possessed a 3 dB bandwidth from 34.5 MHz to 38.6 MHz. Topographs were taken with the incident beam at 45° to the $(0\bar{1}14)$ planes. With the film horizontal, this setting sent the desired diffracted beam normally through the photographic emulsion.

Figure 4.3 shows a stroboscopic topograph of a device being driven by a 37.46 MHz 15 V p/p sine wave applied to the uniform transducer. The main travelling wave generated by the transducer is clearly visible, as is the secondary wave generated by the multistrip coupler. It can be seen that in the multistrip coupler there is a reduction in the intensity of the primary wave and an increase in the intensity of the secondary wave. This corresponds to the transfer of energy from the primary wave to the secondary wave.

Careful inspection of the primary and secondary waves in the multistrip coupler region of Figure 4.3 shows a $\pi/2$ phase shift between the two waves. This can be observed in more detail in Figure 4.4. As mentioned in Chapter 2, a phase difference of $\pi/2$ between the tracks is required for total transfer from one track to the other.

(b) Effect of the Apodized Transducer

Figure 4.5 shows part of the device of Figure 4.2 driven by a 15 V p/p signal applied this time to the apodized transducer. This transducer is designed to

minimize reflection when the device is driven by an input to the uniform transducer. Therefore in Figure 4.5 the reflections are not minimized as they are in Figure 4.3. Diffraction effects are evident at the input in both images but are more pronounced in Figure 4.5. It may be concluded that the design of the apodized transducer is important in reducing these effects. It is also evident in Figure 4.5 that there is not total transfer of the waves across the multistrip coupler when the device is driven from the apodized transducer.

(c) Devices Without Multistrip Couplers

An initial examination was made of six devices without multistrip couplers. These devices had $(01\bar{1}0)$ surface planes and the transducer arrangement was as shown in Figure 4.6. Each device consists of an apodized and a uniform split-finger transducer with periodicities (λ_0) of $98 \mu\text{m}$ and apertures of $20\lambda_0$. Topographs were taken with the incident beam at 45° to the $(01\bar{1}0)$ surface planes. With the film horizontal, this setting sent the $03\bar{3}0$ reflected beam normally through the photographic emulsion. Figure 4.7 shows a stroboscopic topograph of one such device driven by a 37.46 MHz 15 V p/p sine wave applied to the uniform transducer.

(d) The Interaction of the Waves with Grain Boundaries

Figure 4.8 shows a topograph of the device of Figure

4.6. The dark band running from M to N corresponds to a low angle grain boundary within the substrate. This contrast is a consequence of the diffraction geometry for white radiation topographs. Figure 4.10 shows how this results from the images from two parts of the crystal tilted at a slight angle to each other. They can be separated, causing a light band to be present, or they can overlap, as in this case, and result in a dark band appearing. The width of the band depends on the relative tilts of the crystallites.

Different topographs recorded simultaneously on the same emulsion will give different contrast conditions because of their different diffraction vectors. This is demonstrated by the topograph in Figure 4.9 which was recorded simultaneously with that shown in Figure 4.8, but using a different Bragg reflection. The contrast for the subgrain boundary in Figure 4.9 is much more marked compared to the waves than in Figure 4.8.

By inspection of Figure 4.8 it can be seen that there is a change of the phase of the waves as they pass the grain boundary. The change is less marked near the end marked N than it is towards the other end of the defect. The phase change can be observed in much more detail in Figure 4.11. Standing waves excited in the transducer region may be observed as well as the travelling waves. The frequency of the standing waves is four times that of the travelling waves.

If the grain boundary could be considered as an

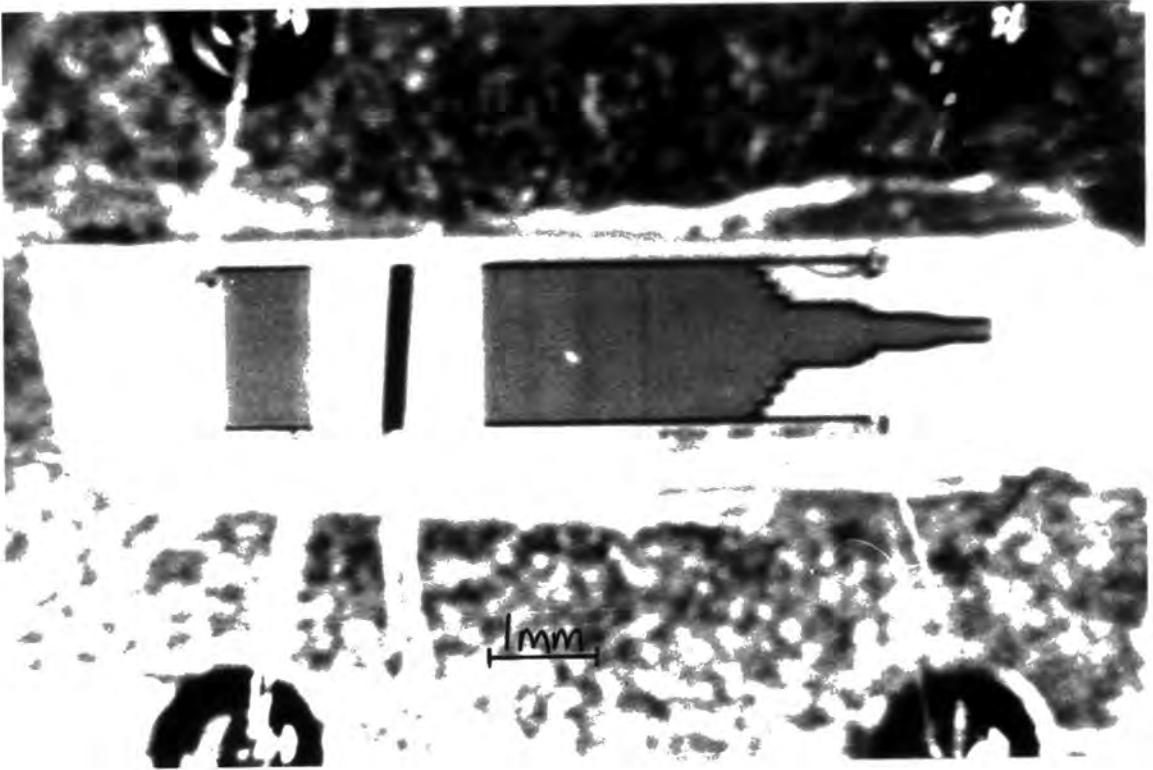


Figure 4.6: Photomicrograph of SAW device without multistrip coupler.

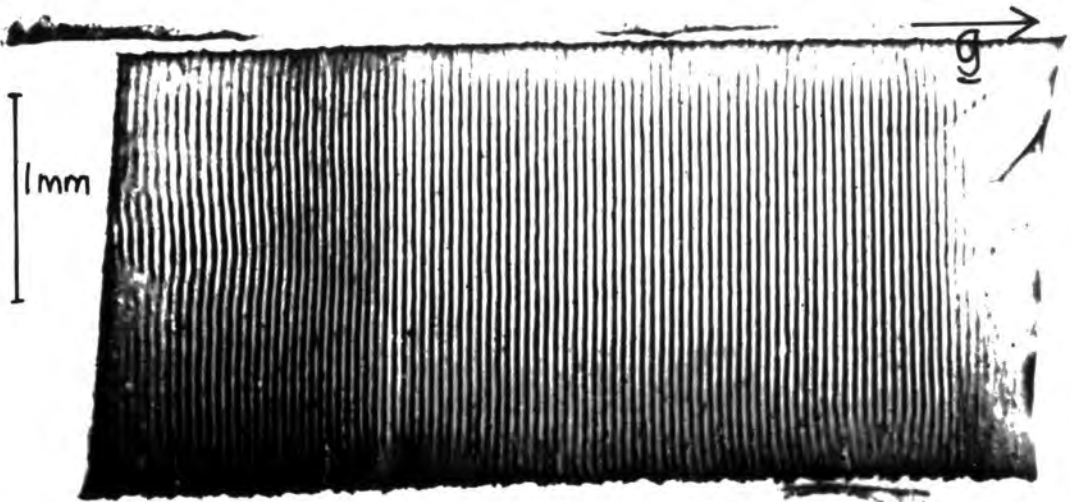


Figure 4.7: Stroboscopic topograph of device similar to Figure 4.6 with 15 V p/p input to uniform transducer.

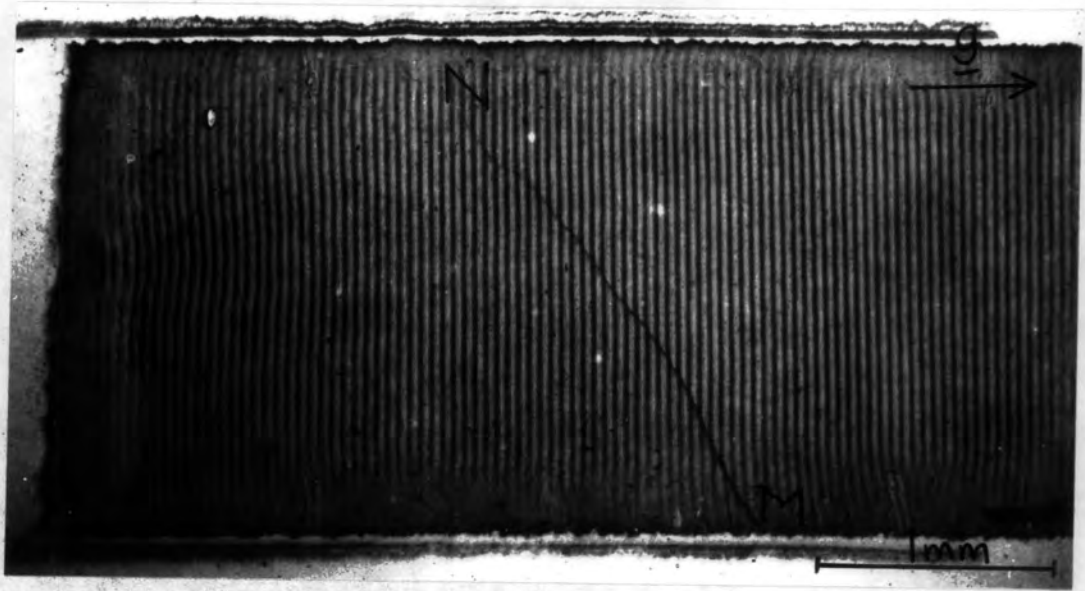


Figure 4.8: Stroboscopic topograph of device of Figure 4.6 with 13 V p/p input to uniform transducer showing low angle grain boundary.

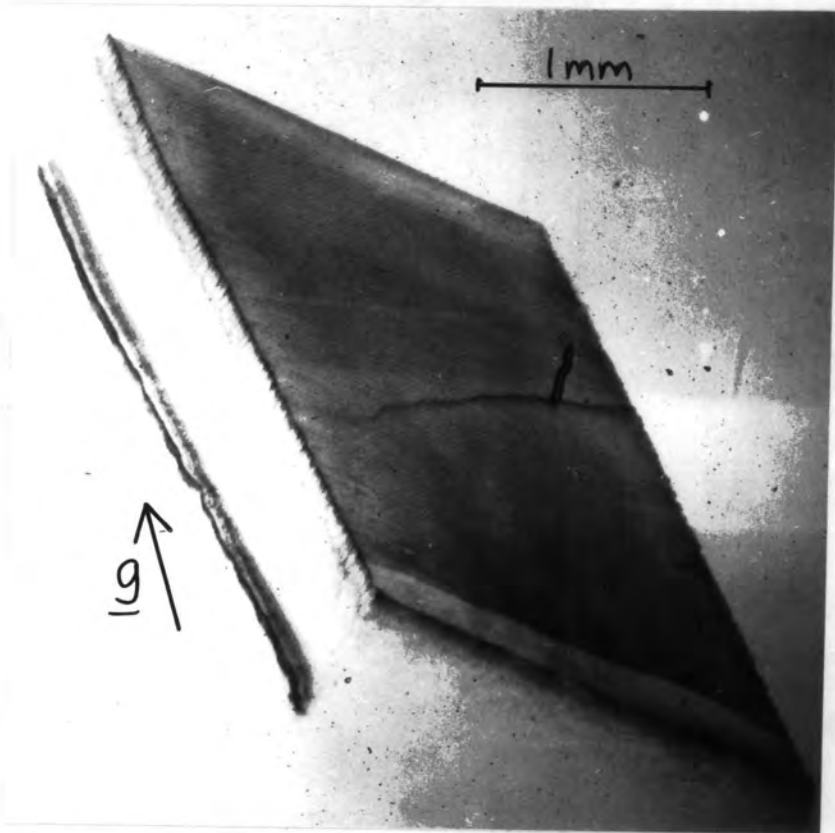


Figure 4.9: Topograph recorded simultaneously with Figure 4.8 but showing different contrast conditions.

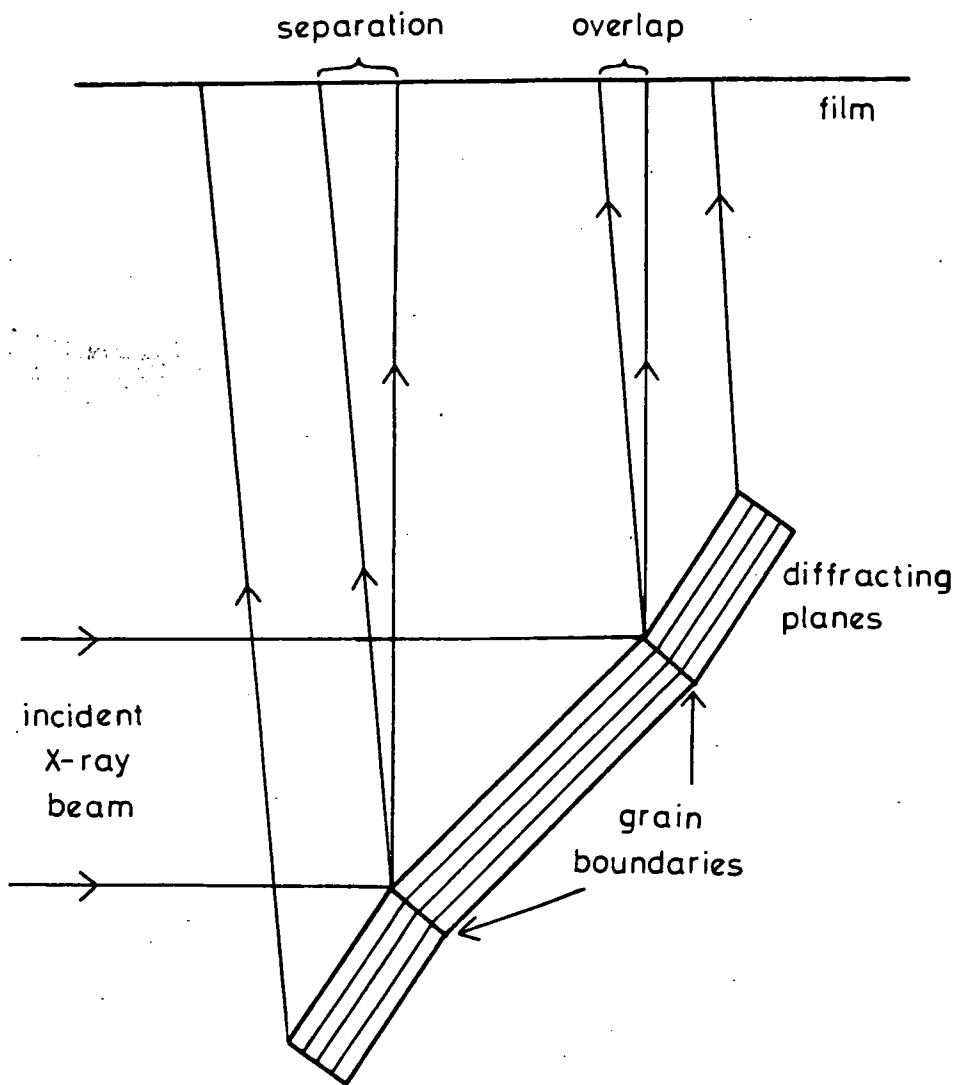


Figure 4.10: Schematic diagram showing how light or dark contrast can occur at low angle grain boundaries. Overlap of images causes a dark band: separation causes a light band.

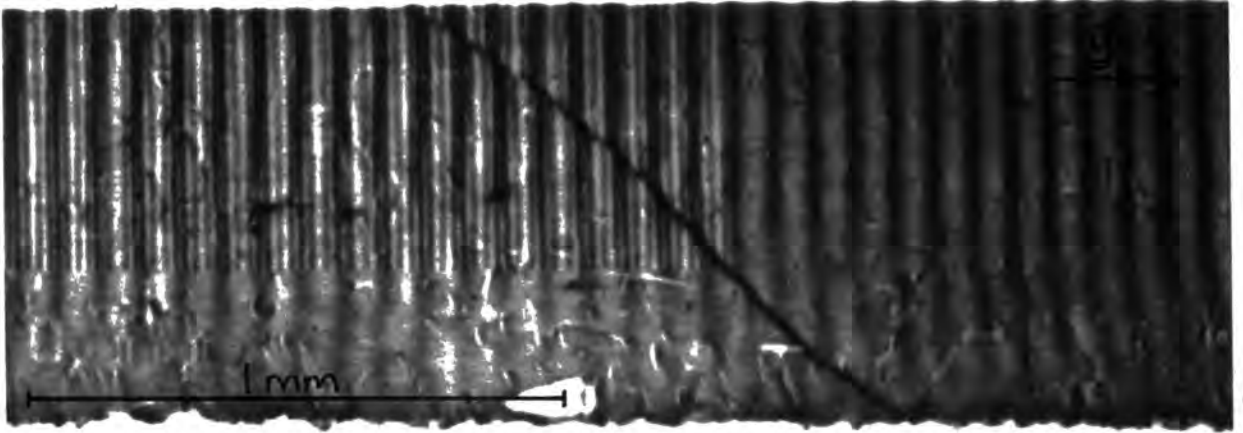


Figure 4.11: Stroboscopic topograph showing phase change at grain boundary. Standing waves in the transducer are also visible.

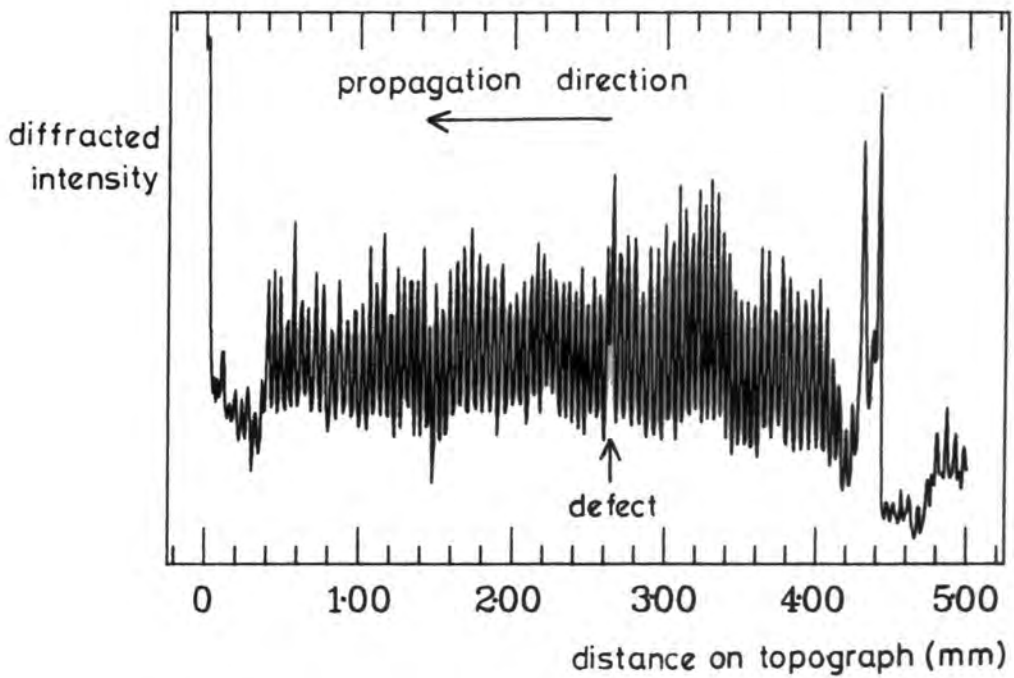


Figure 4.12: Microdensitometer scan of topograph of Figure 4.8.

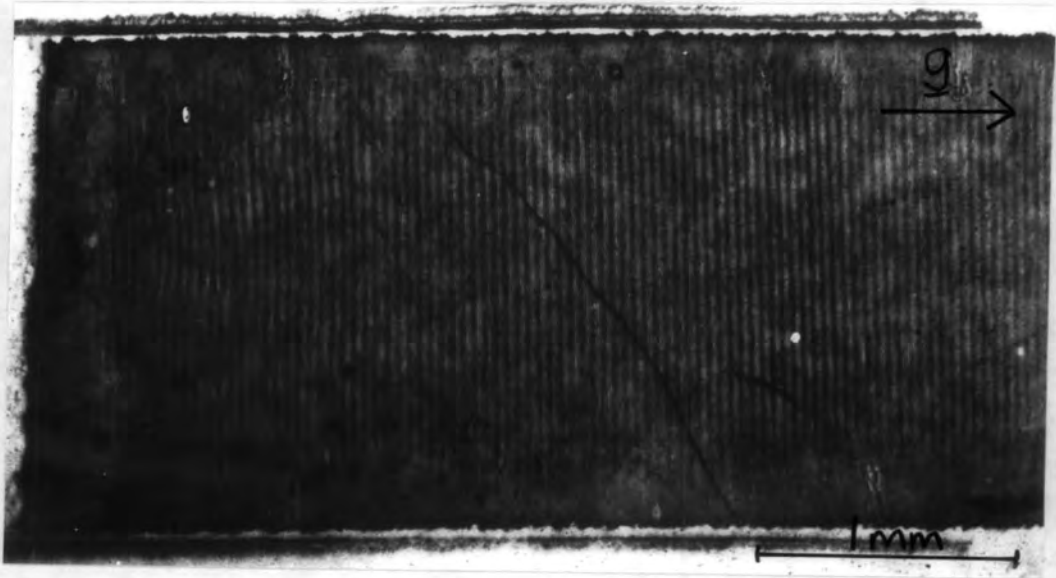


Figure 4.13: Stroboscopic topograph of device of Figure 4.6 with 3V p/p input to uniform transducer.

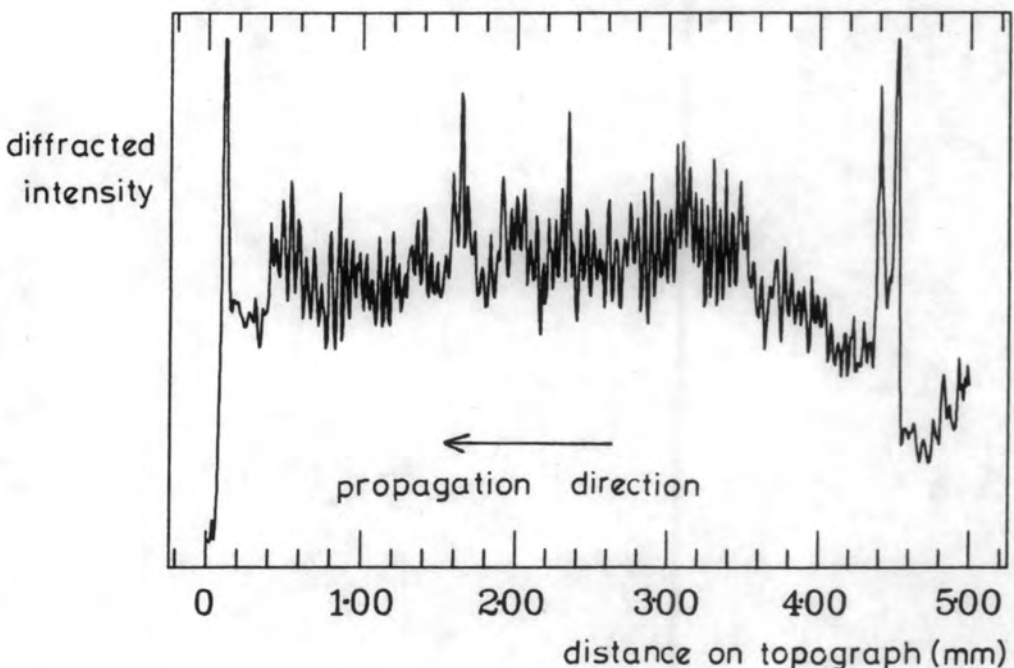


Figure 4.14: Microdensitometer scan of topograph of Figure 4.13.

infinitely thin crack, then the theoretical basis for the investigation of such a defect is already available. The fundamental physics upon which ultrasonic wave propagation and scattering studies are based is well established. Phenomena are studied in the fields of seismology, geophysics, civil and mechanical engineering, high frequency physical electronics, ultrasonic non-destructive testing, sonar and radar. The fundamental aspects of wave propagation and scattering have been presented by many authors [54,55].

Defects like cracks act as the sources of acoustic scattering when illuminated by incident waves and radiate the scattered waves through reflection, diffraction and mode conversion. Hirao et al [56] have analysed the transmitted and reflected Rayleigh waves and compared the solutions with experiments involving edge cracks. Their analysis is restricted to edge cracks normal to the free surface of a homogeneous isotropic half-space and normally incident waves. They show that Rayleigh wave scattering occurs in at least two different manners depending on the depth:wavelength ratio. For a Rayleigh wave of given wavelength λ , their results show that for the transmitted Rayleigh wave there appears to be no significant difference of the phase shift θ_t up to crack depth $d \approx \lambda$. From $d \approx \lambda$ upward θ_t is proportional to d . The reflected Rayleigh wave is subjected to about $\pi/6$ phase delay from $d \approx \lambda$ upwards. In the case of shallow edge cracks or low frequency waves, the

whole crack behaves as an obstacle for the Rayleigh wave propagation. In contrast, the edges and tip of a deep crack introduce a set of discrete geometrical discontinuities which the Rayleigh wave must get beyond to transmit the edge crack. Since the transmitted Rayleigh wave is forced to travel down and up the crack faces, its travelling time increases in correspondence to the detour distance $2d$. Thus the phase change of the SAW's can be explained if the grain boundary structure is thought of as an infinitely thin crack.

There is considerable interference with the uniformity of the wave amplitude across the device due to grain boundaries. This was shown by Goddard et al [25] who made microdensitometer scans parallel to the wavefronts on each side of a boundary, giving the average amplitude of the waves across the device. Figure 4.12 shows the result of a microdensitometer scan of Figure 4.8 taken parallel to the wave propagation direction. It is obvious that where the waves cross the subgrain boundary there is a marked reduction in the energy in the wave, indicating an interaction between the wave and the defect by which energy is incoherently reflected or scattered from the defect.

Figure 4.13 shows a topograph of the same device as Figure 4.8 being driven by an input signal of 3 V p/p applied to the uniform transducer. Figure 4.14 shows the result of a microdensitometer scan of this topograph taken parallel to the wave propagation direction. With the lower

input signal it is more easily observed that there is a modulation of the waves on the device. Modulation is thought to arise from the presence of unfiltered sub-harmonics [50].

Ultrasonic wave propagation theory might also be used to explain the modulation effects if these are more pronounced in devices with defects. Achenbach et al [57] present a simple approximate approach to the scattering of Rayleigh waves by surface-breaking cracks which is valid in the high-frequency range where the crack depth is greater than the Rayleigh wavelength. When an incident Rayleigh wave interacts with a crack, both the mouth and the edge of the crack act as centres of diffraction which generate diffracted body waves and reflected and transmitted Rayleigh surface waves. The diffracted body waves are neglected but the reflected, transmitted and diffracted Rayleigh waves are taken into account.

The solution provides a simple method of determining the crack depth. In the high frequency range both the forward-scattered and back-scattered amplitudes show a modulation with regularly spaced peaks and troughs. This modulation indicates a resonance phenomenon due to the surface motions on the faces of the crack, which suggest that the spacing between either peaks and troughs should be directly related to the crack depth d . If Δk_R is the spacing between successive peaks and troughs of the modulation, then the depth of an edge crack can be

determined from the simple formula

$$d = \pi / \Delta k_R$$

This relation is thought to be valid for $d \gg \lambda$. Further analysis is required to determine whether the modulation effects are due solely to unfiltered subharmonics or whether there is any evidence of more pronounced effects in devices with low angle grain boundaries. Figure 4.14 shows some indication of more obvious modulation after the waves have passed the grain boundary; this would be expected from the above approach since the waves are mainly transmitted across the grain boundary rather than reflected from it.

(e) The Effects of X-ray Wavelength

According to the theory of Cervá and Graeff [51], the wavelength of the X-rays should not affect the contrast of the waves since the reflection can be approximated by a simple mirror reflection from a corrugated surface. Investigations have been made into the contrast of the images for various incident wavelengths. The wavelength was altered by changing the angle of incidence, θ_i , of the radiation, thus altering the Bragg condition for reflection. As the angle θ_i is decreased, the wavelength also decreases. In order to obtain exact wavelength values, the crystal was first set so that the wavelength of the Nb absorption edge was centred on the crystal. This was visible as an abrupt intensity change in the image as shown

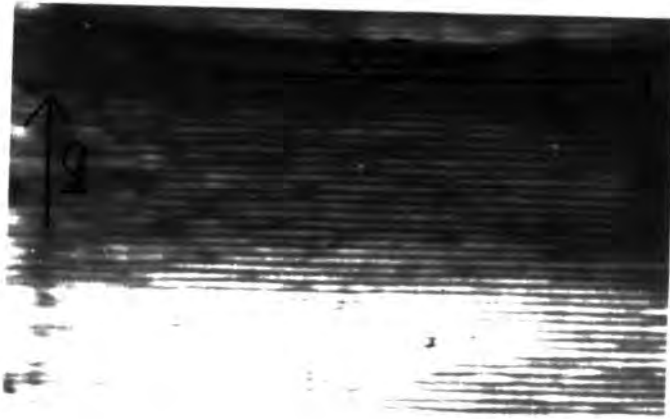


Figure 4.15: Part of stroboscopic topograph of device of Figure 4.6 showing abrupt change in intensity over Nb K-absorption edge.

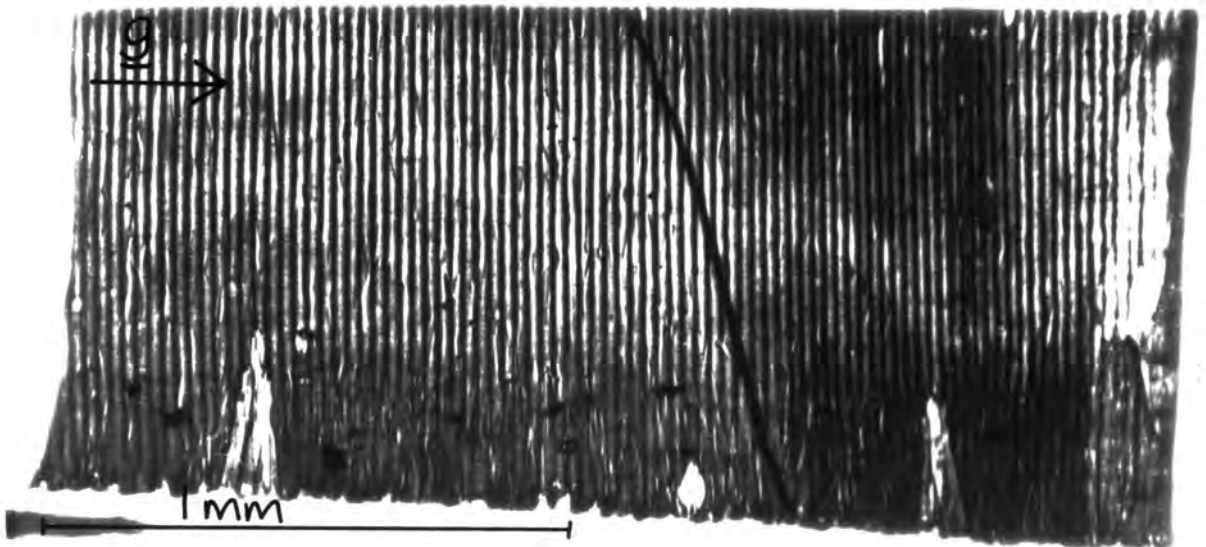


Figure 4.16: Stroboscopic topograph of device of Figure 4.6 using incident wavelength of 1 \AA .

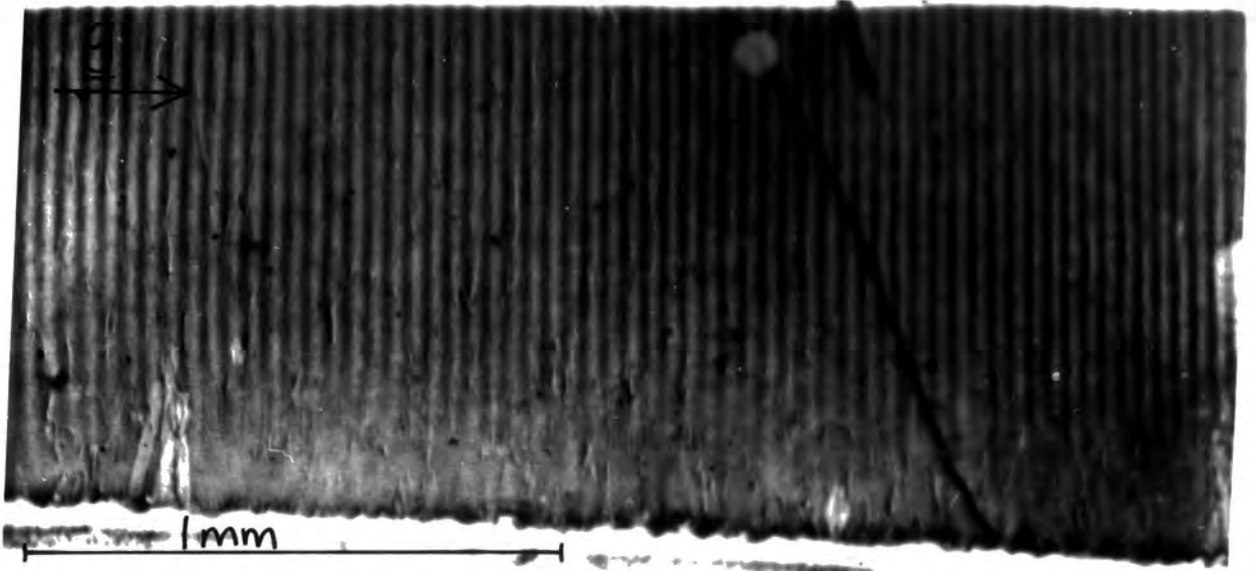


Figure 4.17: Stroboscopic topograph of device of Figure 4.6 using incident wavelength of 1.4 \AA .



Figure 4.18: Stroboscopic topograph of device of Figure 4.6 with 1 V p/p input to uniform transducer.

in Figure 4.15. To enable this to be done more quickly, a TV camera was used as a detector, allowing direct observation of the image. This made possible accurate calibration of the angular setting of the crystal from which other settings were obtained using the angular movement of a goniometer. Topographs were taken for various wavelengths including 0.6, 0.65, 0.7, 0.8, 0.9, 1.0, 1.1, 1.2, and 1.4 Å. All other conditions, including input voltage and specimen-film distance, were kept constant. The results show that contrast does not change significantly with wavelength. However the mark:space ratio appears to decrease as wavelength decreases. This is demonstrated by comparison of Figure 4.15 ($\lambda=0.65$ Å), Figure 4.16 ($\lambda=1$ Å), and Figure 4.17 ($\lambda=1.4$ Å). Figure 4.15 shows a marked decrease in mark:space ratio at wavelengths below the Nb K-absorption edge.

(f) Input Voltage And Contrast

To investigate the effects of input voltage, topographs were recorded for input voltages in the range from 1 V to 15 V p/p. The results show that at higher voltages the contrast of the waves is higher and the dislocations are not observed. At lower voltages the dislocations are seen as well as the waves. This is demonstrated by comparison of Figure 4.18 and Figure 4.7 (page 54). The effects are also evident in Figure 4.3 (page 49) where the primary wave decreases and dislocations are seen in the substrate.

CHAPTER 5: LITHIUM TETRABORATE

As mentioned in Chapter 2, the search continues for materials suitable as substitutes for quartz and lithium niobate for use in SAW devices. These two materials have difficulties in satisfying certain device specifications. For example, the ST-cut of α -quartz exhibits temperature compensation for SAW's but possesses only weak electro-mechanical coupling ($k_s^2 = 1.4 \times 10^{-3}$), making it suitable for broad-bandwidth devices requiring a low insertion loss [58]. On the other hand, Y-cut Z-propagating LiNbO_3 possesses strong SAW coupling ($k_s^2 = 4.8 \times 10^{-2}$) but exhibits a high temperature coefficient of delay ($\text{TCD} = 94 \times 10^{-6} \text{ } ^\circ\text{C}^{-1}$) so that, while it is suitable for broad-bandwidth devices such as IF and reflective array compressive filters [31], it requires external temperature stabilization.

A large number of piezoelectric materials have been examined for their possible applications as SAW substrates [32]. Berlinite [33], lead potassium niobate [34], and lithium tetraborate [35] are the most promising ones reported to date; they are predicted to possess substrate cuts with zero temperature coefficient of delay. Unfortunately, severe difficulties are encountered in the crystal growth of both berlinite and lead potassium niobate.

Work has been done recently [35] to assess lithium

tetraborate, $\text{Li}_2\text{B}_4\text{O}_7$, for SAW applications. The X-cut Z-propagating device orientation has a SAW velocity of 3510 ms^{-1} . The second-order temperature coefficient is about ten times larger than that for ST-quartz, while the observed value of k_s^2 is nine times larger. The temperature variation in delay time is $\pm 60 \text{ ppm}$, compared to $\pm 1840 \text{ ppm}$ for YZ- LiNbO_3 over the same temperature range. This degree of temperature compensation, combined with the SAW coupling factor of 1.2% makes XZ- $\text{Li}_2\text{B}_4\text{O}_7$ ideal for use in moderately broad-bandwidth SAW filters requiring good thermal stability.

Much development of the growth process for $\text{Li}_2\text{B}_4\text{O}_7$ is required before it can be used commercially. Lithium tetraborate is grown using the Czochralski technique. This is a popular method of crystal growth because it can produce large dislocation-free crystals in a relatively short space of time. The melt is kept just above the melting temperature by resistance heating, induction heating, or arc image heating. The melt is held in a crucible of suitable refractory material, for example graphite or quartz, which does not contaminate the crystal material. The seed crystal is dipped into the melt and is withdrawn at a slow steady rate to form an ingot which is often a single crystal. The seed is rotated slowly at about 30 rpm to keep the growing crystal uniform and cylindrical in shape. The diameter of the growing crystal is controlled by the heater power input. If the power is increased the

diameter of the crystal can be made small and a neck can be produced in a growing crystal. Necking is used to produce a single crystal from a polycrystalline seed or to reduce the dislocation density in a growing crystal.

Slices of Czochralski grown single crystals of $\text{Li}_2\text{B}_4\text{O}_7$ have been examined by X-ray topography, using both conventional and synchrotron radiation sources. An analysis of Burgers vectors of dislocations has been made from recorded topographs.

Experimental

Crystals of $\text{Li}_2\text{B}_4\text{O}_7$ were provided by Plessey Research (Caswell) Ltd. An initial survey of perfection was made in three slices of crystal (labelled A, B and C) with areas about 5 cm^2 and thickness about 1 mm. They were polished first with diamond paste and then with Syton to remove surface damage. $\text{Li}_2\text{B}_4\text{O}_7$ is tetragonal with $a=9.47 \text{ \AA}$, $c=10.26 \text{ \AA}$. It has space group $I4_1cd$. The structure factors for various reflections were calculated using the computer program given in Appendix D. They are given in Table 5.1. The very low values of the structure factors, combined with the large areas of crystal to be scanned, resulted in exposure times in the laboratory of the order of 1-2 days for projection topographs. Topographs of the three slices are shown in Figures 5.1, 5.2 and 5.3.

Refln.	θ_B	Wavelength	Structure Factor	Extinction Distance
400	12.1	1	31	314
040	12.1	1	28	354
004	11.2	1	42	234
440	17.3	1	3	2959
$\overline{4}40$	17.3	1	3	3121
$4\overline{4}0$	17.3	1	3	3121
$\overline{4}\overline{4}0$	17.3	1	3	2959
044	16.7	1	30	317
$04\overline{4}$	16.7	1	31	314
$0\overline{4}4$	16.7	1	31	314
$0\overline{4}\overline{4}$	16.7	1	30	317

Table 5.1: Calculated values of structure factors and extinction distances for various reflections from lithium tetraborate (from computer program given in Appendix D).

Crystal A of Figure 5.1 was chosen for further examination. Topographs were recorded using other reflections. Use of white beam synchrotron radiation topography reduced exposure times to an hour or less. This allowed topographs to be recorded faster and so enabled a Burgers vector analysis to be performed more easily.

A wedge of crystal (labelled D) which had originally adjoined slice A was subsequently also examined (see Figure 5.4). Its thickness varied between 3 mm and 8 mm. The low absorption coefficient of $\text{Li}_2\text{B}_4\text{O}_7$ allows crystals as thick as this to be examined under low absorption conditions without further slicing. This facilitates investigation of the dislocations introduced during growth.

Examples of calculations of absorption coefficients are given in Table 5.2.

Linear Absorption Coefficients, μ [59]

	Mo-K α ($\lambda=0.7101$ A)	Cu-K α ($\lambda=1.5418$ A)
Li	0.217	0.716
B	0.392	2.39
O	1.31	11.5

Type of atoms	Li	B	O
Number (N)	2	4	7
Atomic Weight (A.W.)	3	5	8
A.W. \times N	6	20	56
Molecular weight =	82		

$$\frac{\mu}{\rho} = \frac{6}{82} \mu_{\text{Li}} + \frac{20}{82} \mu_{\text{B}} + \frac{56}{82} \mu_{\text{O}}$$

$$\rho = 2.44 \text{ gcm}^{-3}$$

Table 5.2: Calculation of absorption coefficients for lithium tetraborate with Mo K α and Cu K α radiation.

Hence, for Cu-K α radiation, $\mu = 20.713$ and for $\mu t=1$, thickness $t=0.5$ mm. For Mo-K α radiation, $\mu = 2.455$ and for $\mu t=1$, thickness $t=5$ mm. Thus with Mo-K α radiation, 5 mm of material can be examined with absorption such that $\mu t=1$. Thus Mo K α radiation was chosen for projection topographs of crystals A,B and C. Synchrotron white beam radiation was chosen for investigation of crystal D.

Results

Of the three slices examined initially, slice A (Figure 5.1) is by far the most perfect; it has a dislocation density of about 10 cm^{-2} compared to 150 to

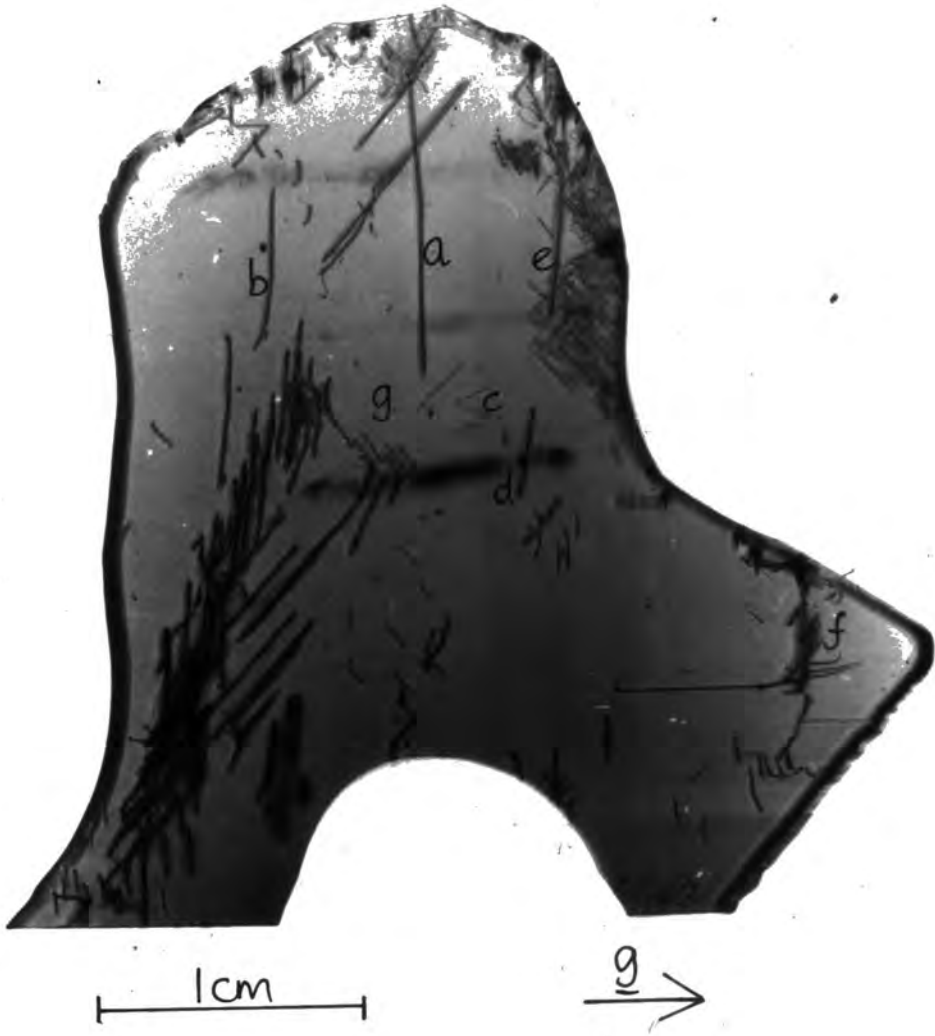


Figure 5.1: Projection topograph of lithium tetraborate (crystal A) using characteristic Mo $K\alpha$ radiation of wavelength 0.7101 \AA and 040 reflection.



Figure 5.2: Projection topograph of lithium tetraborate (crystal B) using characteristic Mo K α radiation of wavelength 0.7101 Å and 040 reflection.

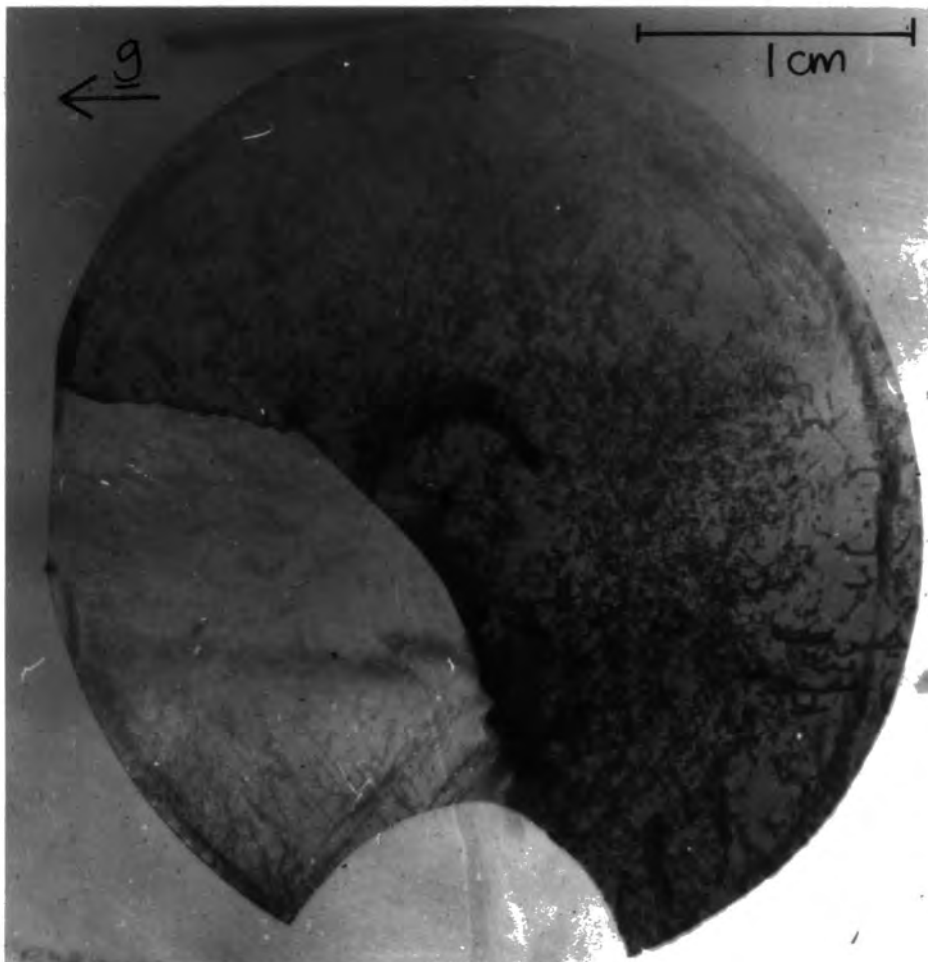


Figure 5.3: Projection topograph of lithium tetraborate (crystal C) using characteristic Mo $K\alpha$ radiation of wavelength 0.7101 \AA and 040 reflection.



Figure 5.4: Synchrotron radiation topographs of lithium tetraborate (crystal D) using 040 reflection and wavelength of 1 Å.

200 cm^{-2} for the other two slices (B and C). It has been chosen for analysis of the Burgers vectors of dislocations introduced during growth from the melt.

Burgers Vectors

As mentioned in Chapter 1, dislocations are characterized by line direction \underline{l} and Burgers vector \underline{b} . Pure screw dislocations are invisible in reflections for which $\underline{g}\cdot\underline{b}=0$. Pure edge dislocations vanish only in reflections for which $\underline{g}\cdot\underline{b}\times\underline{l}$ is also zero, where \underline{l} is the unit vector parallel to the dislocation line. Mixed dislocations do not vanish. The vectors \underline{l} and \underline{b} together determine the geometrical form of the dislocation, its energy, and possible reactions with other defects. It can be shown that most of the energy of dislocations is in the long-range strain field and that this energy is proportional to the square of the Burgers vector [13]. Consequently, energetic considerations dictate that most dislocations have Burgers vectors equal in length to the shortest lattice translation vector. Since $\text{Li}_2\text{B}_4\text{O}_7$ is body-centred, this suggests that the Burgers vectors should be $1/2\langle 111 \rangle$.

Analysis of Crystal A

The dislocations in the topograph of Figure 5.1 have been analysed in an attempt to identify the Burgers vectors. Unfortunately, the geometry of the crystal makes it impossible to obtain the reflections required to make a complete Burgers vector analysis. Because the structure factors for the 440 type reflections are so low it would be impossible to obtain topographs using these reflections. Nevertheless, some dislocation Burgers vectors have been identified. The initial topograph was taken using the 040 reflection. Subsequent topographs used the $00\bar{4}$, 404 and $\bar{4}04$ reflections. The results of examination of these topographs are given in Table 5.3.

Dislocation	Reflection			
	040	$00\bar{4}$	404	$\bar{4}04$
a	p	a	a	a
b	p	p	a	p
c	p(w)	p	p(s)	p(s)
d	p	a	a	a
e	p	a	a	a
f	p	p(w)	a	p(w)
g	a	p	p	p

Table 5.3: Results of examination of topographs of lithium tetraborate (crystal A). Figure 5.1 shows the annotation of the dislocations (a=absent, p=present, s=strong, w=weak).

The following deductions may be made:

(i) Dislocations (a), (d) and (e) are pure screw with Burgers vectors $\underline{b}=[010]$.

(ii) Dislocation (b) is probably pure screw with

$\underline{b} = \pm 1/2[111]$ or $\pm 1/2[\bar{1}\bar{1}\bar{1}]$.

(iii) Dislocation (c) is probably mixed or edge with $\underline{b} = \pm[100]$ or $\pm[001]$.

(iv) Dislocation (f) is probably edge with $\underline{b} = [010]$.

(v) Dislocation (g), which is not seen on Figure 5.1 but is observed in other topographs, is probably screw type with $\underline{b} = \pm[001]$.

(vi) All other dislocations are visible on all the topographs which were recorded. They are most likely to have Burgers vectors $\underline{b} = 1/2\langle 111 \rangle$ because they would be expected to be visible in the topographs taken, as well as this being the shortest lattice vector. The impossibility of taking 440 type reflections because of the low structure factors precludes further analysis of dislocations.

It may be concluded from the above that the dislocations in crystal A are most likely to have Burgers vectors $\underline{b} = 1/2\langle 111 \rangle$, although there are some with $\underline{b} = \langle 100 \rangle$.

Many interesting features may be observed on the topograph of crystal A (Figure 5.1). Firstly, the dislocation images are of width about 200 μm for the 040 reflection used. This is a result of the large extinction distances of about 300 μm , which are given in Table 5.1 (page 69). As mentioned in Chapter 1, the width of a screw dislocation image is:

$$s = \frac{\xi}{2\pi} \underline{g} \cdot \underline{b}$$

For edge dislocations the width is about 1.75 times this. If the width is calculated for a screw dislocation with

$\underline{g}=[040]$ and $\underline{b}=[010]$, then $s \approx 200 \mu\text{m}$ as observed for dislocation (a). For $\underline{b}=1/2[111]$ then $s \approx 100 \mu\text{m}$, as observed for other dislocations.

Of the other features evident in the topographs, the most notable are the intermediary images which can be observed as oscillatory contrast in the lower regions of Figure 5.1. Some of the dislocations also show bimodal intensity profiles, dislocation (a) for example. The bimodal image intensity profile becomes quite obvious in high-order reflections and weak reflections and so should be expected in these topographs. Authier [15] has discussed double images in some detail.

Crystal D

Examination of Figure 5.4 shows the seed crystal and dislocations introduced during growth. Periodic Pendellosung fringes are normally visible in crystals of varying thickness provided that the crystal quality is high enough. Since this is the case for the wedge crystal D, fringes should be observed. However, the visibility of the fringes is reduced because of the large thickness of crystal, as mentioned in Chapter 1, so in this case the fringes cannot be seen.

Figure 5.4 had to be made from two topographs because the crystal was too large to allow a single topograph to be

taken using synchrotron radiation without scanning. These topographs show that slices of lithium tetraborate as thick as 8 mm can be examined using X-ray topography. Further analysis of crystals of this size would provide substantial information about the crystal growth mechanism.

Future Prospects

Crystals B and C are not perfect enough for further work to be considered. However, the perfection of crystal A is so high that it would enable a slice with no dislocations present to be cut from the lower right side of the crystal. Another slice could be cut which had only one dislocation traversing the slice. Model experiments could then be performed by exciting bulk waves in each slice and using stroboscopic X-ray topography to examine the difference in wave propagation when a single dislocation is present. This type of investigation could be of substantial importance in attempts to analyse the effect of dislocations on wave propagation in piezoelectric solids.

CHAPTER 6 : CONCLUSIONS

X-ray topography is undoubtedly a valuable tool in the evaluation of crystal perfection, but the availability of synchrotron radiation has now extended its potential to include topography of thick, low absorption crystals and the imaging of periodic phenomena by stroboscopic techniques.

Stroboscopic white beam topography using synchrotron radiation provides a means for looking at the dynamic behaviour of a large range of phenomena in solids at frequencies between a few MHz and several GHz. This method has been used to investigate the performance of LiNbO_3 SAW devices operating at 38 MHz. The results of the experiments verify the feasibility of synchrotron topography as a means of examining such devices. The energy transfer from the primary to secondary wave in a multistrip coupler has been observed, together with a phase change across the coupler. The ability of the apodized transducer to minimize reflection in a SAW delay line has also been demonstrated. The interaction of waves with a grain boundary structure has been investigated. When the waves pass the defect there is a reduction of energy and considerable disruption of wavefront uniformity which indicates that an interaction is occurring whereby the waves are incoherently scattered by the defect. There is also a change of phase of the waves as they pass the defect. It is suggested that a grain boundary

could be considered as an infinitely thin crack. Ultrasonic wave propagation theory could then be used in the analysis of the interaction. The distance travelled by the waves as they propagate up and down the crack faces would explain the phase change in the waves. Investigation of devices with known depths of grain boundaries would be required to confirm this theory. It is also suggested that ultrasonic wave propagation theory could account for some modulation effects in the waves, but this requires further investigation. The effects of incident X-ray wavelength and input voltage have also been investigated. The mark:space ratio of the waves in the image appears to decrease as wavelength decreases.

Thick specimens of $\text{Li}_2\text{B}_4\text{O}_7$ have been examined using white beam transmission topography. The long exposure times required would have made these investigations impractical in the laboratory. However, the use of synchrotron radiation made a Burgers vector analysis both feasible and easily carried out experimentally. Unfortunately, in practice the extremely low structure factors for some reflections from the crystal precluded a complete Burgers vector analysis. Nevertheless, it may be concluded from the results obtained that the Burgers vectors are most likely to be mainly $1/2\langle 111 \rangle$ with some $\langle 100 \rangle$ present. The high perfection of one of the crystals examined could make it a likely candidate for experiments to investigate the effects of single dislocations on acoustic wave propagation using

stroboscopic X-ray topography.

Stroboscopic X-ray topography using synchrotron radiation offers many possibilities for the investigation of other phenomena. Provided that the phenomenon of interest can be cycled repetitively at frequencies in exact multiples of the ring frequency, a wide range of stroboscopic X-ray diffraction experiments can be envisaged. Some examples might include the study of structural phase transitions induced by application of an electric field or the study of the dynamic strains in working microwave devices operating on piezoelectric GaAs or InP. Periodic phenomena in biological or polycrystalline materials could be analysed. and the technique also has potential for modelling in non-destructive testing applications. Slowed down time-dependent experiments, performed by deliberate detuning of the phase, are another possibility. Finally, piezoelectric beam conditioners could be used to extend and augment the range of frequencies available.

REFERENCES

1. B.K. Tanner (1976), "X-Ray Diffraction Topography", Pergamon, Oxford.
2. A.R. Lang (1970), in "Modern Diffraction and Imaging Techniques in Materials Science", (ed. Amelinckx et al), North Holland, p.407.
3. G.R. Booker (1970), in "Modern Diffraction and Imaging Techniques in Materials Science", (ed. Amelinckx et al), North Holland, p.553.
4. S. Amelinckx (1964), "The Direct Observation of Dislocations", (Solid State Physics Supplement 6), Academic Press, N.Y.
5. A.R. Lang (1958), J. Appl. Phys., 29, 597.
6. A.R. Lang (1959), Acta Cryst., 12, 249.
7. A.R. Lang (1957), Acta Cryst., 10, 839.
8. Z.G. Pinsker (1978), "Dynamical Scattering of X-Rays in Crystals", Springer, Berlin.
9. B.W. Batterman and H. Cole (1964), Rev. Mod. Phys., 36, 681.
10. A. Authier (1970), in "Advances in Structure Research by Diffraction Methods" (ed. Brill and Mason), 3, 1.
11. C. Kittel (1976), "Introduction to Solid State Physics", 5th. ed., Wiley, N.Y., p.190.
12. D. Hull (1975), "Introduction to Dislocations", Pergamon, Oxford.
13. J.P. Hirth and J. Lothe (1968), "Theory of Dislocations", McGraw-Hill, N.Y.
14. A.R. Lang (1967), in "Advances in X-Ray Analysis", vol.10, Plenum, N.Y., p.97.
15. A. Authier (1967), in "Advances in X-Ray Analysis", vol.10, Plenum, N.Y., p.9.
16. A. Authier (1970), in "Modern Diffraction and Imaging Techniques in Materials Science", (ed. Amelinckx et al), North Holland, p.481.

17. P.B. Hirsch, A. Howie, R.B. Nicholson, D.W. Pashley, and M.J. Whelan (1965), "Electron Microscopy of Thin Crystals", Butterworths, London, p.251.
18. W. Gudat and C. Kunz (1979), in "Synchrotron Radiation, Techniques and Applications", (ed. C. Kunz), Topics in Physics Vol.10, Springer, Berlin, p.55.
19. T. Tuomi, K. Naukkarinen, and P. Rabe (1974), Phys. Stat. Sol.(a), 25, 93.
20. L.G. Shultz (1954), Trans. AIME, 200, 1082.
21. A. Guinier and J. Tennevin (1949), Acta Cryst., 2, 133.
22. U. Bonse (1980), in "Characterization of Crystal Growth Defects by X-Ray Methods", (ed. Tanner and Bowen), Plenum, N.Y., p.298.
23. J. Miltat and M. Kleman (1979), J. Appl. Phys., 50, 7695.
24. M. Hart (1980), in "Characterization of Crystal Growth Defects by X-Ray Methods", (ed. Tanner and Bowen), Plenum, N.Y., p.421.
25. P.A. Goddard, G.F. Clark, B.K. Tanner and R.W. Whatmore (1983), Nucl. Instr. Meth., 208, 705.
26. C.-C. Gluer, W. Graeff, and H. Moller (1983), Nucl. Inst. Meth., 208, 701.
27. H. Bradazcek, G. Hildebrandt, D. Jahnig, J.D. Stephenson and W. Graeff (1983), Nucl. Instr. Meth., 208, 719.
28. "Surface Acoustic Waves", (ed. Oliner), Topics in Applied Physics, Springer, Berlin, 1978.
29. A.E.H. Love (1927), "Mathematical Theory of Elasticity", University Press, Cambridge.
30. A.W. Warner (1965), Proc. Ann. Freq. Control Symp., 25, 104.
31. M.G. Holland and T.C. Lewis (1974), Proc. IEEE, 62, 581.
32. R.W. Whatmore (1980), J. Cryst. Growth, 48, 530.
33. D.G. Morency, W. Soluch, J.F. Vetelino, S.D. Middleman, D. Harmon, S. Surek, J.C. Field, G. Lehmann (1978), Appl. Phys. Lett., 33, 117.

34. R.M. O'Connell (1975), J. Appl. Phys., 49, 3324.
35. R.W. Whatmore, N.M. Shorrocks, C. O'Hara, F.W. Ainger and I.M. Young (1981), Elect. Lett., 17, 11.
36. F.G. Marshall and E.G. Paige (1971), Elect. Lett., 7, 460.
37. F.G. Marshall and E.G. Paige (1971), Elect. Lett., 7, 463.
38. C. Maerfeld (1976), Wave Electronics, 2, 82.
39. W.J. Spencer (1968), in "Physical Acoustics", vol. V, (ed. Mason and Thurston), Academic Press, N.Y.
40. C.H. Palmer (1973), J. Acoust. Soc. Am., 53, 948.
41. R.J. Gerdes and C.E. Wagner (1971), Proc. Ann. Freq. Control Symp., 25, 118.
42. W.J. Spencer (1966), J. Acoust. Soc. Am., 39, 929.
43. O. Berolo and D. Butler (1977), Proc. IEEE Ultrasonics Symposium, p.98.
44. B.A. Richardson and G.F. Kino (1970), Appl. Phys. Lett., 16, 82.
45. Y. Nakagawa, K. Yamanouchi, and K. Shibayama (1974), J. Appl. Phys., 45, 2817.
46. G. Eberharter and H. Feuerbaum (1980), Appl. Phys. Lett., 37, 698.
47. R.W. Whatmore, P.A. Goddard, B.K. Tanner, and G.F. Clark (1982), Nature, 299, 44.
48. R.W. Whatmore, P.A. Goddard, and B.K. Tanner (1982), Proc. IEEE Ultrasonics Symposium, vol. I, p.363.
49. D.K. Bowen, G.F. Clark, S.T. Davies, J.R.S. Nicholson, K.J. Roberts, J.N. Sherwood and B.K. Tanner (1982), Nucl. Instr. Meth. 195, 277.
50. B.K. Tanner (1983), in "The Application of Synchrotron Radiation to Problems in Materials Science", Proc. Study Weekend 13-14 November 1982, Daresbury Laboratory Reports, p.66.
51. H. Cerva and W. Graeff (1984), Phys. Stat. Sol. (a) 82, 35.

52. H. Cerva and W. Graeff (1985), Phys. Stat. Sol. (a) 87, 507.
53. U. Bonse (1964), Z. Phys. 177, 385.
54. W.M. Ewing, W.S. Jardetsky and W. Press (1957), "Elastic Waves in Layered Media", McGraw-Hill, N.Y.
55. K.F. Graff (1975), "Wave Motion in Elastic Solids", Clarendon Press, Oxford.
56. M. Hirao, H. Fukuoka, and Y. Miura (1982), J. Acoust. Soc. Am., 72, 602.
57. J.D. Achenbach, A.K. Gautesen and A.D. Mendelsohn (1980), IEEE Trans SU-27, 124.
58. M. Feldmann and J. Henaff (1977), Rev. Phys. Appl., 12, 1775.
59. "International Tables for X-ray Crystallography", Vol. III, 2nd. ed., Reidel, Holland, 1983.

APPENDIX A

Crystal Cuts Of Lithium Niobate

Two cuts of LiNbO_3 crystals were used in the devices examined by stroboscopic X-ray topography, as illustrated in Figure A1. A very common cut is Y-cut LiNbO_3 , so called because the plane normal is in the Y-direction shown in Figure A1. The surface plane is $(01\bar{1}0)$. "128° niobate" is so called because the angle between the surface plane and the $(01\bar{1}0)$ plane is 127.86° . The surface plane is $(0\bar{1}14)$.

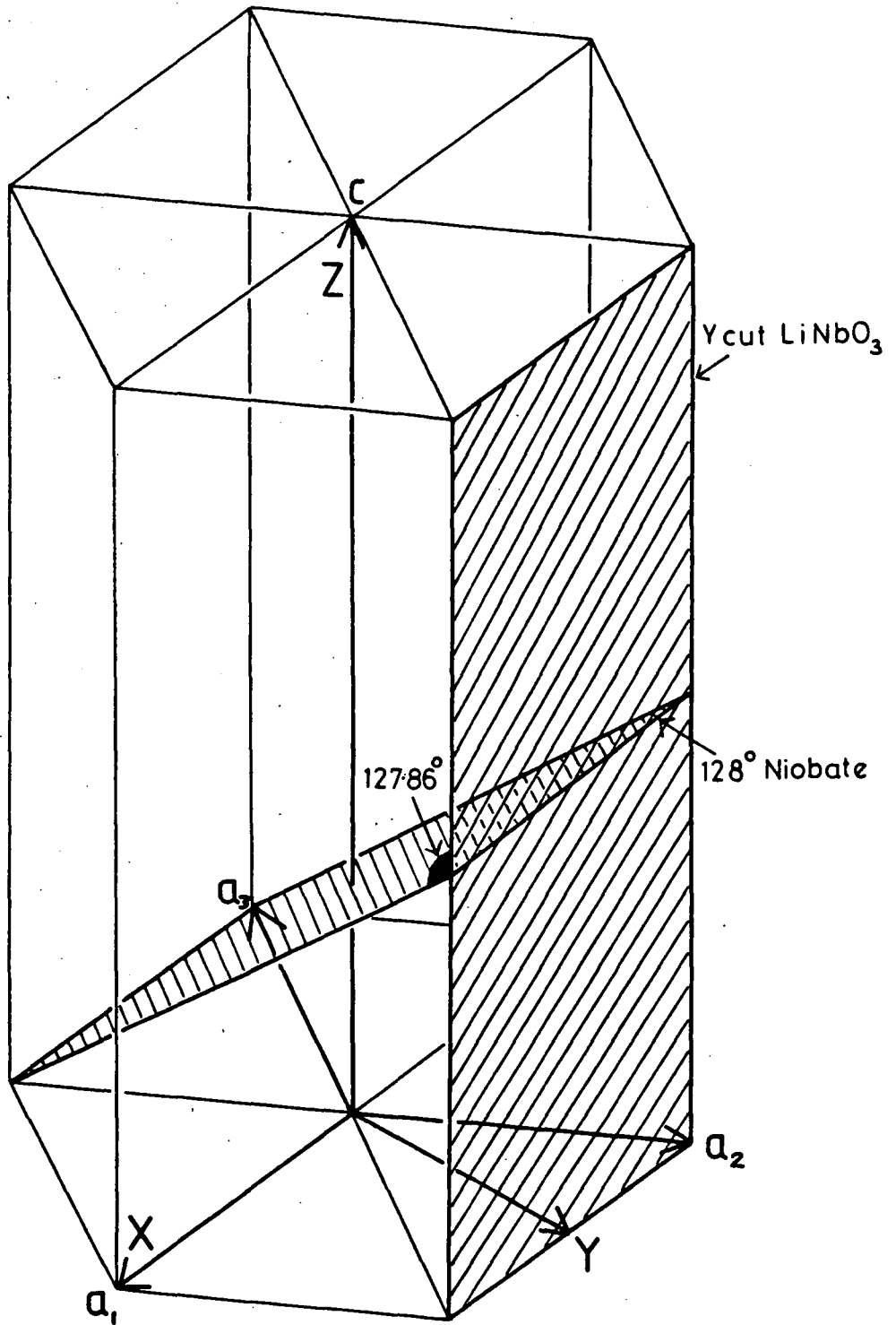


Figure A1: Diagram showing orientation of surface planes used in the SAW devices examined.

APPENDIX B

A computer program in BASIC for use on a BBC microcomputer is listed below; it constructs a model of the image which would be seen on a photographic plate if a LiNbO_3 SAW device was placed in a white radiation X-ray beam at 45° to the beam direction.

```

10 *****
20 REM LINB (4.6.84) JANEY CRINGEAN,DURHAM
30 *****
40 :
50 *****
60 REM 90 DEGREE REFLECTION LAUE,03-30,LITHIUM NIOBATE
70 *****
80 :
90 MODEO
100 DATA *1,1.12820,3.95460,0.750800,1.05240,0.617500,85.3
905,0.465300,168.261,0.037700,*2,17.6142,1.18865,12.0144,11.
7660,4.04183,0.204785,3.53346,69.7957,3.75591,*3,3.04850,13.
2771,2.28680,5.70110,1.54630,0.323900,0.86700,32.9089,0.2508
110 DATA *4,1,0,0,0.355,*5,1,0,0,-0.355,*6,2,0,0,0.145,*7,
2,0,0,-0.145,*8,3,0.31,0.01,0.25,*9,3,-0.01,0.30,0.25,*10,3,
-0.30,-0.31,0.25,*11,3,-0.31,-0.01,-0.25,*12,3,0.01,-0.30,-0
120 DIM T(10),X(10),Y(10),Z(10),A(10),a(10),B(10),b(10),C(
10),c(10),D(10),d(10),E(10),F(10)
130 :
140 PROCAskinput
150 FOR R%=1 TO 2
160 PROCPrintscreen
170 FOR A%=-Max% TO Max%
180 FOR B%=0 TO Max%
190 C%=-A%-B%
200 FOR D%=-Max% TO Max%
210 IF (-A%+B%+D%)/3=(-A%+B%+D%)DIV3 THEN PROCPlot

220 NEXT:NEXT:NEXT
230 IF R%=2 THEN PROCPrint
240 PRINTTAB(68,22) "Press":PRINTTAB(64,23) "P for hard
copy":PRINTTAB(64,24) "ESCAPE to quit";
250 REPEAT:A$=GET$:UNTIL A$="P" OR A$="p"
260 NEXT
270 END
280 :
290 DEFPROCAskinput
300 CLS:PRINT "90 Degree reflection Laue pattern , 03-30 ,
Lithium Niobate"
310 PRINT "-----"

320 INPUT"" "Enter crystal-film distance (cm.)";S
330 INPUT"" "Enter maximum index""(suggest not > 7)";Max%

340 INPUT"" "Enter maximum reflection modulus""(suggest no
t > 56)";Sum%
350 INPUT"" "Do you want reflection indices displayed (Y/N)
";T$
360 INPUT"" "Do you want intensities and extinction distanc
es calculated (Y/N)";F$
370 Xcentre=630:Ycentre=505
380 AD=5.147:CD=13.856
390 H%=0:K%=1:L=-3.1
400 ENDPROC
410 :
420 DEFPROCPrintscreen
430 CLS
440 IF R%=2 THEN Xsize=355:Ysize=214:Xscale=0.01069:Yscale

```

```

=0.01765 ELSE Xsize=266:Ysize=274:Xscale=0.0143:Yscale=0.013
68
450 MOVE Xcentre+Xsize,Ycentre+Ysize
460 FOR I%=-1 TO 1 STEP 2
470   FOR J%=-1 TO 1 STEP 2
480     DRAW I%*Xsize+Xcentre,I%*J%*Ysize+Ycentre
490     NEXT NEXT
500 PRINTTAB(12,1);"90 Degree reflection Laue , 03-30 ,
Lithium Niobate"
510 PRINTTAB(10,31);"Max. index ";Max%;", Max. modulus ";
Sum%;", Crystal-film distance ";S;"cm.";
520 ENDPROC
530 :
540 DEFPROCPlot
550 HexA=FNHex(A%,B%,D%)
560 IF HexA*HexA>Sum% OR HexA=0 THEN ENDPROC
570 CosPhi=(H%*A%+K%*B%+.5*(H%*B%+K%*A%)+3*AD*AD*D%*L/CD/
CD/4)/FNHex(H%,K%,L)/HexA
580 Phi=ACS(CosPhi)
590 IF Phi=0 OR (Phi>=PI/2 AND Phi<=PI) THEN ENDPROC
600 TanPhi=TAN(Phi)
610 TanPsi=TAN(2*Phi)
620 Ad=A%
630 Bd=(2*B%+A%)/SQR(3)
640 Dd=D%*AD/CD
650 Hd=H%
660 Kd=(2*K%+H%)/SQR(3)
670 Ld=L*AD/CD
680 Xnew=(Ad*Hd+Bd*Kd+Dd*Ld)/FNMod(Hd,Kd,Ld)
690 IF Hd=0 AND Kd=0 THEN Ynew=Ad ELSE Ynew=(Bd*Hd-Ad*Kd)
/SQR(Hd*Hd+Kd*Kd)
700 IF Hd=0 AND Kd=0 THEN Znew=Bd ELSE Znew=(Dd*(Hd*Hd+Kd
*Kd)-Bd*Kd*Ld-Ad*Hd*Ld)/SQR(Hd*Hd+Kd*Kd)/FNMod(Hd,Kd,Ld)
710 IF Znew=0 THEN ENDPROC
720 Xs=Ynew/Znew/Xscale*S
730 Ys=Xnew/Znew/Yscale*S*TanPhi/TanPsi
740 IF ABS(Xs)>Xsize OR ABS(Ys)>Ysize THEN ENDPROC
750 Xs=Xs+Xcentre
760 Ys=Ys+Ycentre
770 IF R%=2 THEN PLOT 69,Xs,Ys:ENDPROC
780 IF T$="N" OR T$="n" THEN PLOT 69,Xs,Ys:ENDPROC
790 IF F$="Y" OR F$="y" THEN PROCCalculate:PRINTTAB(66,10)
;"Intensity":PRINTTAB(66,11);IN:PRINTTAB(66,13);"Ext. Dist. (m
ic)":PRINTTAB(66,14);EX:PRINTTAB(66,16);"Wavelength(A)":PRIN
TTAB(66,17);WL;
800 PRINTTAB(66,8);A%;B%;C%;D%:PRINTTAB(66,22);"Press any"
:PRINTTAB(66,23);"key to":PRINTTAB(66,24);"continue";
810 REPEAT:A$=INKEY$(1):PLOT 70,Xs,Ys:Now=TIME:REPEAT:UNTI
L TIME>Now+10:PLOT 69,Xs,Ys:Now=TIME:REPEAT:UNTIL TIME>Now+1
0:UNTIL A$<>" "
820 PLOT 69,Xs,Ys
830 PRINTTAB(66,8);" " :PRINTTAB(66,10);" " "
PRINTTAB(66,11);" " :PRINTTAB(66,13);" "
" :PRINTTAB(66,14);" " :PRINTTAB(66,16);" "
" :PRINTTAB(66,17);" "
840 PRINTTAB(66,22);" " :PRINTTAB(66,23);" " :P
RINTTAB(66,24);" " ;
850 ENDPROC

```

```

860  DEFFNHex(X,Y,Z)=SQR(X*X+Y*Y+X*Y+3*AD*AD/CD/CD/4*Z*Z)
870  :
880  DEFFNMod(X,Y,Z)=SQR(X*X+Y*Y+Z*Z)
890  :
900  DEFPROCPrint
910  *FX7,7
920  *FX5,2
930  *FX8,7
940  *FX6,0
950  CHAIN "P.NEWDUMP"
960  ENDPROC
970  :
980  DEFPROCCalculate
990  PROCReaddata
1000 DS=1/SQR(4*(A%^2+B%^2+A%*B%)/3/AD^2+D%^2/CD^2)
1010 Theta=PI/2-Phi
1020 SinTheta=SIN(Theta)
1030 WL=2*DS*SinTheta
1040 SJ=SinTheta/WL
1050 SR=0:SI=0
1060 FOR I=1 TO 10
1070   F(I)=A(I)*EXP(-a(I)*SJ^2)+B(I)*EXP(-b(I)*SJ^2)+C(I)*
EXP(-c(I)*SJ^2)+D(I)*EXP(-d(I)*SJ^2)+E(I)
1080   ARG=2*PI*(H%*X(I)+K%*Y(I)+L%*Z(I))
1090   SR=SR+F(I)*COS(ARG):SI=SI+F(I)*SIN(ARG)
1100   NEXT
1110 IN=SR^2+SI^2
1120 EX=PI*317.89*COS(Theta)/0.2818/SQR(IN)/WL
1130 ENDPROC
1140 :
1150 DEFPROCReaddata
1160 FOR I=1 TO 10
1170   K$=" "+STR$(I+3)
1180   RESTORE 110
1190   REPEAT:READ A$:UNTIL A$=K$
1200   READ T(I),X(I),Y(I),Z(I)
1210   NEXT
1220 FOR I=1 TO 10
1230   K$=" "+STR$(T(I))
1240   RESTORE
1250   REPEAT:READ A$:UNTIL A$=K$
1260   READ A(I),a(I),B(I),b(I),C(I),c(I),D(I),d(I),E(I)
1270   NEXT
1280 ENDPROC

```

APPENDIX C

Two computer programs in BASIC for use on a BBC microcomputer are listed below; they construct models of back-reflection Laue photographs (program LAUE1 for hexagonal crystals, program LAUE2 for cubic crystals).

```

10 *****
20 REM LAUE1 (2.5.84) JANEY CRINGEAN, DURHAM
30 *****
40 :
50 *****
60 REM BACK REFLECTION LAUE FOR HEXAGONAL SYSTEMS
70 *****
80 :
90 MODEO
100 :
110 PROCAskinput
120 FOR R%=1 TO 2
130 PROCPrintscreen
140 FOR A%=-Max% TO Max%
150 FOR B%=0 TO Max%
160 FOR D%=-Max% TO Max%
170 C%=-A%-B%
180 PROCPlot
190 NEXT:NEXT:NEXT
200 IF R%=2 THEN PROCPrint
210 PRINTTAB(68,20) "Press":PRINTTAB(64,21) "P for hard
copy":PRINTTAB(64,22) "ESCAPE to quit";
220 REPEAT:A$=GET$:UNTIL A$="P" OR A$="p"
230 NEXT
240 END
250 :
260 DEFPROCAskinput
270 CLS:PRINT "Back reflection Laue pattern , hexagonal cr
ystal"
280 PRINT "-----"
290 INPUT "Enter indices of reflection" "H";H%:INPUT "K
";K%:INPUT "I";I%:INPUT "L";L%
300 INPUT "Enter crystal-film distance (cm.)";S
310 INPUT "Enter maximum index" "(suggest not > 7)";Max%
320 INPUT "Enter maximum reflection modulus" "(suggest no
t > 56)";Sum%
330 INPUT "Enter lattice parameters (Angstroms)" "A";AD
:INPUT "C";CD
340 INPUT "Do you want reflection indices displayed (Y/N)
";T$
350 Xcentre=630:Ycentre=505
360 ENDPROC
370 :
380 DEFPROCPrintscreen
390 CLS
400 IF R%=2 THEN Xsize=426:Ysize=328:Xscale=0.01069:Yscale
=0.01765 ELSE Xsize=320:Ysize=420:Xscale=0.0143:Yscale=0.013
68
410 MOVE Xcentre+Xsize,Ycentre+Ysize
420 FOR I%=-1 TO 1 STEP 2
430 FOR J%=-1 TO 1 STEP 2
440 DRAW I%*Xsize+Xcentre,I%*J%*Ysize+Ycentre
450 NEXT:NEXT
460 PRINTTAB(17,1);"Back reflection Laue (hexagonal) : ";
H%" ";K%" ";I%" ";L%"
470 PRINTTAB(0,31);"Max. index ";Max%;", Max. modulus ";S

```

```

um%;", Crystal-film distance ";S;"cm., A=";AD;", C=";CD;
480 ENDPROC
490 :
500 DEFPROCPlot
510 HexA=FNHex(A%,B%,D%)
520 IF HexA*HexA>Sum% OR HexA=0 THEN ENDPROC
530 CosTheta=(H%*A%+K%*B%+.5*(H%*B%+K%*A%)+3*AD*AD*D%*L%/
CD/CD/4)/FNHex(H%,K%,L%)/HexA
540 IF CosTheta=0 OR CosTheta=1 OR CosTheta=-1 THEN ENDPR
OC
550 TanTheta=SQR(1-CosTheta^2)/CosTheta
560 TanPhi=TAN(2*ATN(TanTheta))
570 Ad=A%
580 Bd=(2*B%+A%)/SQR(3)
590 Dd=D%*AD/CD
600 Hd=H%
610 Kd=(2*K%+H%)/SQR(3)
620 Ld=L%*AD/CD
630 Xnew=(Ad*Hd+Bd*Kd+Dd*Ld)/FNMod(Hd,Kd,Ld)
640 IF Xnew=0 THEN ENDPROC
650 IF Hd=0 AND Kd=0 THEN Ynew=Ad ELSE Ynew=(Bd*Hd-Ad*Kd)
/SQR(Hd*Hd+Kd*Kd)
660 IF Hd=0 AND Kd=0 THEN Znew=Bd ELSE Znew=(Dd*(Hd*Hd+Kd
*Kd)-Bd*Kd*Ld-Ad*Hd*Ld)/SQR(Hd*Hd+Kd*Kd)/FNMod(Hd,Kd,Ld)
670 Xs=Ynew*TanPhi/Xnew/TanTheta/Xscale*S
680 Ys=Znew*TanPhi/Xnew/TanTheta/Yscale*S
690 IF ABS(Xs)>Xsize OR ABS(Ys)>Ysize THEN ENDPROC
700 Xs=Xs+Xcentre
710 Ys=Ys+Ycentre
720 PLOT 69,Xs,Ys
730 IF R%=2 THEN ENDPROC
740 IF T$="Y" OR T$="y" THEN PRINTTAB(70,10);" " :PR
INTTAB(70,10);A%;B%;C%;D%:PRINTTAB(70,12);"Press any":PRINTT
AB(70,13);"key to":PRINTTAB(70,14);"continue";:A$=GET$
750 ENDPROC
760 :
770 DEFFNHex(X,Y,Z)=SQR(X*X+Y*Y+X*Y+3*AD*AD/CD/CD/4*Z*Z)
780 :
790 DEFFNMod(X,Y,Z)=SQR(X*X+Y*Y+Z*Z)
800 :
810 DEFPROCPrint
820 *FX7,7
830 *FX5,1
840 *FX8,7
850 *FX6,0
860 CHAIN "P.NEWDUMP"
870 ENDPROC

```

```

10 *****
20 REM LAUE2 (1.5.84) JANEY CRINGEAN, DURHAM
30 *****
40 :
50 *****
60 REM BACK REFLECTION LAUE FOR CUBIC SYSTEMS
70 *****
80 :
90 MODE 0
100 :
110 PROCAskinput
120 FOR R%=1 TO 2
130 PROCPrintscreen
140 FOR A%=-Max% TO Max%
150 FOR B%=-Max% TO Max%
160 FOR C%=0 TO Max%
170 IF Type$="SC" THEN PROCPlot
180 IF Type$="BCC" AND (A%+B%+C%)/2=(A%+B%+C%)DIV2
THEN PROCPlot
190 IF Type$="FCC" AND (A%+B%)/2=(A%+B%)DIV2 AND (
A%+C%)/2=(A%+C%)DIV2 AND (B%+C%)/2=(B%+C%)DIV2 THEN PROCPlot
200 NEXT:NEXT:NEXT
210 IF R%=2 THEN PROCPrint
220 PRINTTAB(68,20)"Press":PRINTTAB(64,21)"P for hard co
py":PRINTTAB(64,22)"ESCAPE to quit";
230 REPEAT:A$=GET$:UNTIL A$="P" OR A$="p"
240 NEXT
250 END
260 :
270 DEFPROCAskinput
280 CLS:PRINT "Back Reflection Laue Pattern"
290 PRINT "-----"
300 INPUT "'Enter indices of reflection"'"H";H%:INPUT"K"
;K%:INPUT"L";L%
310 INPUT "'Enter crystal-film distance (cm.)";S
320 INPUT "'Enter maximum index"'"(suggest not > 7)";Max%
330 INPUT "'Enter maximum (h^2+k^2+l^2)"'"(suggest not >
56)";Sum%
340 INPUT "'Do you want reflection indices displayed (Y/N)
";T$
350 Xcentre=630:Ycentre=505
360 PRINT "'Enter crystal type"'"(S=Simple cubic,F=FCC,B
=BCC)"
370 Endproc=FALSE
380 REPEAT
390 A$=GET$
400 IF A$="F" OR A$="f" THEN Type$="FCC":Endproc=TRUE
410 IF A$="B" OR A$="b" THEN Type$="BCC":Endproc=TRUE
420 IF A$="S" OR A$="s" THEN Type$="SC":Endproc=TRUE

430 UNTIL Endproc
440 ENDPROC
450 :
460 DEFPROCPrintscreen
470 CLS
480 IF R%=2 THEN Xsize=426:Ysize=328:Xscale=0.01069:Yscale
=0.01765 ELSE Xsize=320:Ysize=420:Xscale=0.0143:Yscale=0.013
68

```

```

490 MOVE Xcentre+Xsize,Ycentre+Ysize
500 FOR I%=-1 TO 1 STEP 2
510   FOR J%=-1 TO 1 STEP 2
520     DRAW I%*Xsize+Xcentre,I%*J%*Ysize+Ycentre
530     NEXT: NEXT
540 PRINTTAB(22,0);"Back Reflection Laue : ";H%" ";K%" ";L
%
550 PRINTTAB(9,31);Type$;","Max index:";Max%;","Max (h^2+k^2
+l^2):";Sum%;","Crystal-film distance:";S;"cm.";
560 ENDPROC
570 :
580 DEFPROCPlot
590 ModA=FNMod(A%,B%,C%)
600 IF ModA*ModA>Sum% OR ModA=0 THEN ENDPROC
610 CosPhi=(H%*A%+K%*B%+L%*C%)/FNMod(H%,K%,L%)/ModA
620 IF CosPhi=0 OR CosPhi=1 OR CosPhi=-1 THEN ENDPROC
630 TanPhi=SQR(1-CosPhi^2)/CosPhi
640 TanPsi=TAN(2*ATN(TanPhi))
650 Xnew=(A%*H%+B%*K%+C%*L%)/FNMod(H%,K%,L%)
660 IF Xnew=0 THEN ENDPROC
670 IF H%=0 AND K%=0 THEN Ynew=A% ELSE Ynew=(B%*H%-A%*K%)/
SQR(H%*H%+K%*K%)
680 IF H%=0 AND K%=0 THEN Znew=B% ELSE Znew=(C%*(H%*H%+K%*
K%)-B%*K%*L%-A%*H%*L%)/SQR(H%*H%+K%*K%)/FNMod(H%,K%,L%)
690 Xs=Ynew/Xnew/Xscale*S*TanPsi/TanPhi
700 Ys=Znew*TanPsi/Xnew/TanPhi/Yscale*S
710 IF ABS(Xs)>Xsize OR ABS(Ys)>Ysize THEN ENDPROC
720 Xs=Xs+Xcentre
730 Ys=Ys+Ycentre
740 IF R%=2 THEN PLOT 69,Xs,Ys:ENDPROC
750 IF T$="N" OR T$="n" THEN PLOT 69,Xs,Ys:ENDPROC
760 PRINTTAB(70,10);A%;B%;C%:PRINTTAB(70,12);"Press any":P
RINTTAB(70,13);"key to":PRINTTAB(70,14);"continue";
770 REPEAT:A$=INKEY$(1):PLOT 70,Xs,Ys:Now=TIME:REPEAT:UNTI
L TIME>Now+10:PLOT 69,Xs,Ys:Now=TIME:REPEAT:UNTIL TIME>Now+1
0:UNTIL A$<>" "
780 PLOT 69,Xs,Ys
790 PRINTTAB(70,10);"          ":PRINTTAB(70,12);"          ":P
RINTTAB(70,13);"          ":PRINTTAB(70,14);"          ";
800 ENDPROC
810 :
820 DEFFNMod(X,Y,Z)=SQR(X*X+Y*Y+Z*Z)
830 :
840 DEFPROCPrint
850 *FX7,7
860 *FX5,1
870 *FX8,7
880 *FX6,0
890 CHAIN "P.NEWDUMP"
900 ENDPROC

```

APPENDIX D

A computer program in BASIC for use on a BBC microcomputer is listed below; it calculates structure factors and extinction distances for $\text{Li}_2\text{B}_4\text{O}_7$ crystals.

```

10 *****
20 REM LTB (14.8.84) JANEY CRINGEAN, DURHAM
30 *****
40 :
50 *****
60 REM STRUCTURE FACTORS FOR
70 REM LITHIUM TETRABORATE
80 *****
90 :
100 DATA 1,0.158,0.158,0.860,1,-0.158,0.158,0.360,1,0.158,
0.342,0.110,1,0.158,0.658,0.610,1,-0.158,-0.158,-0.860,1,0.1
58,-0.158,0.360,1,-0.158,0.658,0.110,1,-0.158,0.342,0.610
110 DATA 2,0.081,0.169,0.194,2,-0.081,0.169,0.694,2,0.169,
0.419,0.444,2,0.169,0.581,0.944,2,-0.081,-0.169,-0.194,2,0.0
81,-0.169,0.694,2,-0.169,0.581,0.444,2,-0.169,0.491,0.944
120 DATA 2,0.115,-0.054,0.083,2,-0.115,-0.054,0.583,2,-0.0
54,0.385,0.333,2,-0.054,0.615,0.833,2,-0.115,0.054,-0.083,2,
0.115,0.054,0.583,2,0.054,0.615,0.333,2,0.054,0.385,0.833
130 DATA 3,0.135,0.283,0.260,3,-0.135,0.283,0.760,3,0.283,
0.365,0.510,3,0.283,0.635,0.010,3,-0.135,-0.283,-0.260,3,0.1
35,-0.283,0.760,3,-0.283,0.635,0.510,3,-0.283,0.365,0.010
140 DATA 3,0.179,0.067,0.150,3,-0.179,0.067,0.650,3,0.067,
0.321,0.400,3,0.067,0.679,0.900,3,-0.179,-0.067,-0.150,3,0.1
79,-0.067,0.650,3,-0.067,0.679,0.400,3,-0.067,0.321,0.900
150 DATA 3,-0.060,0.157,0.171,3,0.060,0.157,0.671,3,0.157,
0.560,0.421,3,0.157,0.440,0.921,3,0.060,-0.157,-0.171,3,-0.0
60,-0.157,0.671,3,-0.157,0.440,0.421,3,-0.157,0.560,0.921
160 DATA 3,0,0,0,3,0.5,0.5,0,3,0,0.5,0.25,3,0.5,0,0.25
170 :
180 DATA *1,1.12820,3.95460,0.750800,1.05240,0.617500,85.3
905,0.465300,168.261,0.037700
190 DATA *2,2.05450,23.2185,1.33260,1.02100,1.09790,60.349
8,0.706800,0.140300,-0.19320
200 DATA *3,4.19160,12.8573,1.63969,4.17236,1.52673,47.017
9,-20.307,-0.01404,21.9412
210 :
220 DIM T(52),X(52),Y(52),Z(52),H(10),K(10),L(10),WL(10),
AU(52),AL(52),BU(52),BL(52),CU(52),CL(52),DU(52),DL(52),E(52
),F(52),SR(10),SI(10),SF(10),Theta(10),S(10),Degrees(10),Ext
(10)
230 :
240 PROCAskinput
250 :
260 PROCReaddata
270 :
280 PROCCalculate
290 :
300 PROCOutput
310 :
320 END
330 :
340 :
350 DEFPROCAskinput
360 A=9.47
370 C=10.26
375 CLS
380 INPUT "Enter number of reflections (not > 10) ";N

```

```

390 PRINT "'Enter H,K,L values and wavelengths "
400 FOR J=1 TO N
410 PRINT
420 INPUT "H";H(J):INPUT "K";K(J):INPUT "L";L(J):INPUT "
Wavelength (Angstroms)";WL(J)
430 NEXT J
440 PRINT "'PLEASE WAIT"
450 ENDPROC
460 :
470 DEFPROCReaddata
480 RESTORE
490 FOR I=1 TO 52
500 READ T(I),X(I),Y(I),Z(I)
510 NEXT I
520 FOR I=1 TO 52
530 K$="*"+STR$(T(I))
540 RESTORE
550 REPEAT:READ A$:UNTIL A$=K$
560 READ AU(I),AL(I),BU(I),BL(I),CU(I),CL(I),DU(I),DL(I)
,E(I)
570 NEXT I
580 ENDPROC
590 :
600 DEFPROCCalculate
610 FOR J=1 TO N
620 S(J)=0.25*((H(J)^2+K(J)^2)/A^2+L(J)^2/C^2)
630 SinTheta=SQR(S(J))*WL(J)
640 IF SinTheta>1 THEN NEXT J
650 Theta(J)=ASN(SinTheta)
660 Degrees(J)=(INT(10*DEG(Theta(J))))/10
670 SR(J)=0:SI(J)=0:SF(J)=0
680 FOR I=1 TO 52
690 F(I)=AU(I)*EXP(-AL(I)*S(J))+BU(I)*EXP(-BL(I)*S(J))+C
U(I)*EXP(-CL(I)*S(J))+DU(I)*EXP(-DL(I)*S(J))+E(I)
700 ARG=2*PI*(H(J)*X(I)+K(J)*Y(I)+L(J)*Z(I))
710 SR(J)=SR(J)+F(I)*COS(ARG)
720 SI(J)=SI(J)+F(I)*SIN(ARG)
730 NEXT I
740 SF(J)=SQR(SI(J)^2+SR(J)^2)
750 Ext(J)=PI*920.126034*COS(Theta(J))/0.2818/SF(J)/WL(J)

760 NEXT J
770 ENDPROC
780 :
790 DEFPROCOutput
800 CLS
805 PRINT "' LITHIUM TETRABORATE"
810 PRINT "' H K L Angle Wave l. St.Fac. Ext.Dist."
820 FOR J=1 TO N
830 PRINT:PRINT;TAB(1)H(J);TAB
(3)K(J);TAB(5)L(J);TAB(8)Degrees(J);TAB(15)WL(J);TAB(23)INT(
SF(J));TAB(31)INT(Ext(J))
840 NEXT J
850 ENDPROC

```

